Degradation of alkali-activated Fe-rich slag in sulfuric acid

Nana Wen[a], Arne Peys[b], Tobias Hertel[a], Ziyou Yu[c], Dimitrios Sakellariou[c], Yiannis Pontikes[a]

[a] KU Leuven Department of Materials Engineering, Kasteelpark Arenberg 44, 3001 Leuven, Belgium

[b] Sustainable Materials Management, VITO, Boeretang 200, 2400, Mol, Belgium

[c] KU Leuven, M2S, cMACS, Celestijnenlaan 200F, 3001 Heverlee, Belgium

Corresponding author: nana.wen@kuleuven.be

Highlights

- H_2SO_4 resistance of Fe-rich alkali-activated material affected by slag chemistry

- Higher sulfuric acid resistance with increasing Al/Si, Ca/Si and Mg/Ca

- The corroded layer's integrity and slag reaction degree control resistance

- The attack is diffusion-controlled and forms gypsum and silica gel

Abstract

Alkali-activated Fe-rich non-ferrous metallurgical slag (AA-NFS), within the FeO_x-SiO_2-Al_2O_3-CaO-MgO system, were tested in 2 wt.% sulfuric acid for 6 months. Corrosion depth and rate were measured non-destructively by micro X-ray computed tomography. Both intact and corroded areas were characterized by XRD, FTIR, SEM-EDX and NMR. AA-NFS with higher Ca/Si showed a higher resistance to sulfuric acid. The presence of Mg negatively affected the resistance, whereas higher Al concentrations slightly enhanced the resistance in the investigated chemical composition range. The corrosion degree is highly related to the NFS reaction extent in AA-NFS, and this corrosion process is diffusion-controlled. Leaching of the elements (Al, Ca, Mg, Fe and Na) leaves behind mostly silica-rich gels, causing the failure of the framework structure after long-term exposure. The leached Ca^{2+} reacted with SO_4^{2-} in acid

25   solution and formed expansive sulfate products, which clog pores and offer an additional

26   protective barrier for AA-NFS against sulfuric acid.

27 ## Graphical abstract
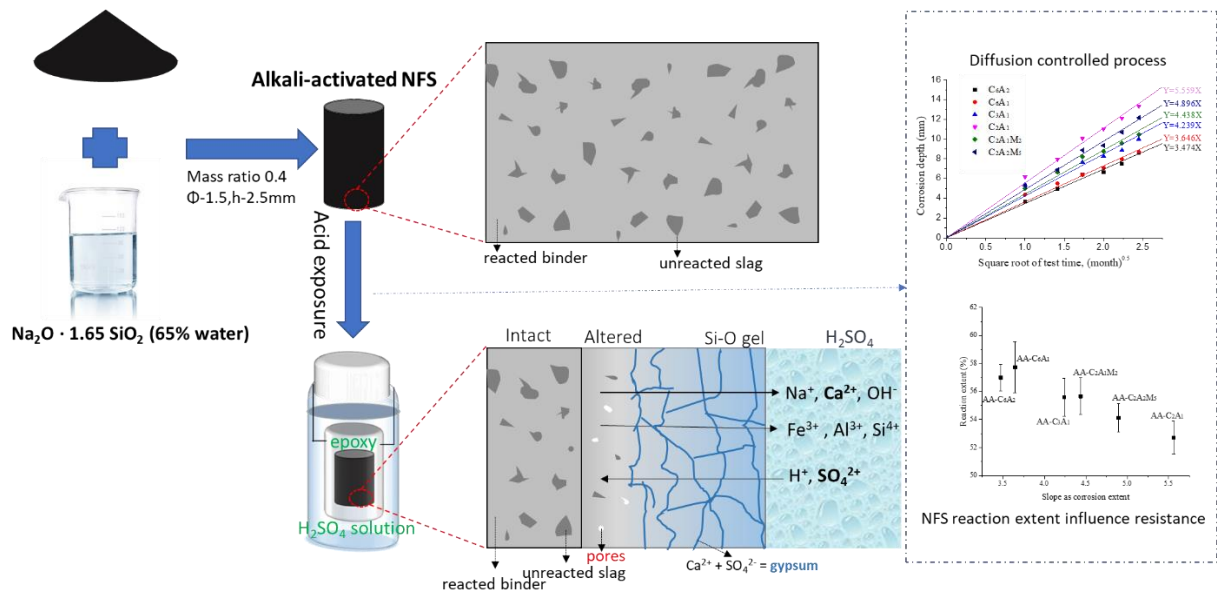
28

29

30 ## Keywords

33 ## 1. Introduction

34   Alkali-activated materials (AAM) have received significant research interest over the past

35   decades due to the lower CO_2 emissions [1], less raw materials processing requirements [2],

36   and better mechanical properties [3]. Fly ash and ground granulated blast furnace slag (GGBFS)

37   are the most widely used precursors in AAM synthesis. The Fe-rich non-ferrous metallurgical

38   Fe-rich slag (NFS), a diverse and abundant Fe-rich resource with Si as well as Al as minor

39   constituents, is an emerging material attracting special interest for AAM synthesis [4]. In

40   previous research work, NFS was already proven to have the possibility to be alkali-activated

41   and exhibited promising mechanical properties [5] and fire resistance [6]. In addition, recent

42   advances have improved the understanding of the role of Fe in the alkali-activated NFS (AA-

43   NFS) and the microstructure of AA-NFS [7-9]. For the particular slags of the current study, the

44   work of Peys et. al [7] is highly relevant: the authors studied AA-NFS using pair distribution

45   function analysis and Mössbauer spectroscopy, reporting Fe in two separate phases after

46   polymerization depending on the Fe oxidation stage. One contains Fe^{2+}, situated in octahedral

47   configuration, and is arranged as trioctahedral layers. The other contains Fe^{3+} which can,

48   similar to Al^{3+}, act as a network former. However, there have been few developments in terms

49   of practical applications. One of the reasons relates to the uncertainty regarding durability. To

50   future-proof AA-NFS, it is necessary to look into their durability performance. There is no one-

51   size-fits-all approach for all durability aspects. Moreover, particular applications typically ask

52   for particular performance, and it might as well be the result of such studies that the new

53   materials developed excel in very specific conditions. This would open the door to niche

54   markets and enable indeed NFS valorization.

55

56   Sulfuric acid is commonly present in sewage systems [10], rocks or soils that contain pyrite or

57   marcasite [11], and industrial processes. Sulfuric attack poses a considerable threat to

58   construction materials [12]. A nanoscale analysis by X-ray pair distribution function analysis

59   found sulfuric acid may cause the disintegration of the main binder gel of the alkali-activated

60   GGBFS paste [13]. Hence, in order to increase the chance of NFS valorization and commercial

61   use as a precursor for alkali-activated materials, the sulfuric acid resistance of AA-NFS must

62   be assessed. But what is the best possible starting slag chemistry?

63

64   It has been found that the increasing content of Al in the AAM system increased the mechanical

65   properties [14] and improved durability, partially because of the improved reactivity [15] and

66   decreased porosity. Furthermore, it was found that the extent of acid attack could be expressed

67   by the Ca dissolution for cement [16]. In many review papers on the durability of AAM [17,

68   18], the AAM system has been classified into three categories according to the Ca content or

69   availability: Ca-free, low-Ca, and Ca-rich. The different types exhibit different reaction

70   mechanisms, reaction products and mechanical properties [18]. The main reaction products for

71   Ca-free, low-Ca and Ca-rich systems are N-A-S-H, (C-N)-A-S-H and C-A-S-H, respectively

72   [19]. It is reported that the acid resistance of N-A-S-H and (C-N)-A-S-H is higher than that of

73   C-A-S-H due to the deleterious formation of expansive gypsum and ettringite in the C-A-S-H

74   gel. Koenig et al. [20] stated that for low-Ca AAM, acid resistance decreases with increasing

75   Ca content of the binder. These findings highlight the importance of Ca content in the system.

76   As an unconventional AA-NFS system characterized by low Ca content (0.5-20%) and elevated

77   Fe levels (40-60%) [21], the impact of Ca on acid resistance remains an open question that

78   needs to be answered. Adediran et al. [22] investigated a co-binder system by blending NFS

79   with ladle slag and GGBFS to introduce additional Al and Ca content. Their results indicated

80   that these co-binders altered the formed gels and enhanced sulfuric acid resistance. However,

81   their study utilized industrial slag, making it challenging to assess the specific effects of Ca

82   and Al. Additionally, the detailed degradation mechanism remains undisclosed. On the other

83   hand, Mg content in the slag is another significant parameter for the microstructure, phase

84   assemblage [23] and durability of AAM [24]. Previous research [19] has shown that the

85   addition of MgO in the AAM system mainly leads to the formation of hydrotalcite-group

86   minerals ($[Mg_{1-x}Al_xOH][OH, \frac{1}{2}CO_3] \cdot mH_2O$), brucite ($Mg(OH)_2$), magnesium silicate hydrate

87   (M-S-H), or magnesium (hydroxy-)carbonates. Also in some cases [25, 26], there are no

88   specific crystalline phases identified. Different Mg-containing phases can affect AAM in

89   different ways. The presence of brucite improves sulfuric acid resistance by increasing acid

90   neutralization capacity and/or polyvalent cationic stabilization [27]. Higher amounts of Mg in

91   hydrotalcite-group minerals favor a larger reaction extent [28] and higher durability

92   performance [24]. However, compared to other elements like Al and Ca, the impact of the Mg

93   content received little attention in literature.

94

95   Previous work [29] concluded that the corrosion mechanism of AAM in sulfuric acid is to a

96   large extent comprised of two sequential reactions: the first step is an ion-exchange process

97   among cations in the AAM framework (Na^+, Ca^{2+}) and the ions (H^+ or H_3O^+) in the acid

98   solution, along with an electrophilic attack of the Si-O-Al bond which could release the

99   tetrahedral aluminum and leave behind a siliceous gel. In the second step, the leached Ca^{2+}

100 diffuses towards the solution and reacts with the sulfate anions in the acid solution, leading to

101 the formation of gypsum in the corroded layers. The expansive gypsum generates internal

102 stresses and induces spalling or cracking, resulting in the failure of the framework [30].

103 However, the degradation mechanisms of AA-NFS when exposed to sulfuric acid solution have

104 not been addressed at all. Apart from the different precursors, the methodology to address the

105 question can be also revisited.

106

107 In the majority of works [31, 32], measuring the degradation degree is commonly done by

108 evaluating mass loss, as this is a simple, fast, and non-destructive method. On the other hand,

109 this approach is nonconclusive with respect to the occurring phenomena, as it is sensitive to

110 other processes that can change the sample mass, such as water absorption, precipitation of

111 gypsum, or insoluble salts [33]. Another widely used indicator is compressive strength change

112 [32]. Correlating this performance indicator to durability is also complex due to the increasing

113 strength of the undamaged area [31, 34] and the significant dimensional changes during the

114 test. In fact, both approaches discussed above are purely indirect evaluations, as no information

115 on the microstructure changes is revealed. Hence, in order to extract a more mechanistic

116 understanding of the sulfuric acid resistance of AA-NFS, corrosion depth is used more and

117 more frequently in AAM research as it can be measured very precisely [12] [31]. The authors

118 of [31] investigated both mass change and corroded depth for AAM samples after exposure to

119 sulfuric acid and found that corroded depth is a more effective measurement of degradation

120 degree compared to mass change. This is because AAM is a highly connected silicate structure.

121 After acid attack, there is a reaction product layer formed on the sample surface. It is apparently

122 intact and contributes to the mass of the specimen but is physically porous and weak [31]. Thus

123 mass change cannot predict the degree of degradation very well.

124

125 Compared to the previous studies [12] [31] where a vernier caliper was used to indicate the

126 deterioration depth (and thus the degradation degree), μ-CT (micro-Computed Tomography)

127 was applied in this work to measure the corroded depth more precisely. For the μ-CT

128 measurement, there is no extra drying or cleaning process involved which may damage or alter

129 the pore structure. Additionally, this non-destructive technique will also provide insights on

130 the microstructure itself, and how that changes over time. The aim of this work is to investigate

131 the effect of the chemical composition of NFS on the sulfuric acid resistance of AA-NFS and

132 to understand the degradation mechanisms of sulfuric acid attack for this novel Fe-rich AAM.

133 To efficiently study the chemical composition of NFS on the acid resistance of alkali-activated

134 NFS, 6 synthetic slags were produced, with varying Al_2O_3, CaO and MgO concentrations under

135 the same FeO_x/SiO_2 molar ratio, and thus 6 AA-NFS were synthesized to enable a comparative

136 assessment. Paste samples were exposed to sulfuric acid, and corrosion degradation was

137 evaluated using corroded depth that was precisely measured by μ-CT. After that, samples were

138   characterized by SEM-EDX, XRD, FTIR and NMR analysis to investigate the degradation

139   mechanisms.

2. Materials and methods

141   The chemicals used for the slag synthesis include iron (III) oxide, metallic iron, quartz,

142   magnesium oxide and calcium oxide (all having a purity >99%), with the chemical

143   compositions chosen to represent industrial NFS. The mixture was melted in an induction

144   furnace (Indutherm TF4000) at 1250 ± 20 °C. This temperature was intentionally set around

145   100 °C higher than the liquidus temperature estimated using FactSage. The molten process

146   lasted for 30 minutes under an atmosphere of CO/CO_2 at 2 (volume ratio). The melt was

147   subsequently quenched in water to obtain a highly amorphous phase content. The slag was then

148   dried at 105 °C for 2 days, and milled to a Blaine surface of 4000 ± 300 cm^3. The detailed

149   synthetic route can be found in previous research work [5, 35]. The chemical composition of

150   the slags is presented in Table 1. The slags are named by the molar ratio of the Al_2O_3 (A), CaO

151   (C) and MgO (M) contents after normalization to the SiO_2 content in the slag. In particular,

152   C_6A_2 and C_6A_1 were designed with the hope of revealing the influence of Al concentrations.

153   The effect of Ca in the system was studied by comparing C_6A_1, C_3A_1 and C_2A_1. In addition, to

154   investigate the influence of Mg on the acid resistance, another two slags $C_2A_1M_2$ and $C_2A_2M_5$,

155   with low and high Mg concentration, were produced. Compared to C_3A_1, , 4 wt% CaO was

156   replaced by MgO to obtain $C_2A_1M_2$. In addition, compared to C_6A_2, 10 wt% CaO was replaced

157   by MgO to obtain $C_2A_2M_5$. After melting and quenching, all the synthetic slags presented high

158   amorphous content (>95 wt% with max 4 wt% olivine), except for $C_2A_2M_5$, which is 82 wt%

159   amorphous, with 17 wt% olivine and 1 wt% hercynite. The XRD pattern and phase assemblage

160   of all slags is shown in Appendix Figure A.1 and Table A.1.

161 *Table 1 Chemical composition of slags (mol%)*

Sample code	FeO	SiO$_2$	CaO	Al$_2$O$_3$	MgO	Formula of slag
C$_6$A$_2$	40	33	20	7	0	F$_{1.2}$S$_1$C$_{0.6}$A$_{0.2}$
C$_6$A$_1$	41	35	19	5	0	F$_{1.2}$S$_1$C$_{0.6}$A$_{0.1}$
C$_3$A$_1$	45	38	12	5	0	F$_{1.2}$S$_1$C$_{0.3}$A$_{0.1}$
C$_2$A$_1$	48	39	8	5	0	F$_{1.2}$S$_1$C$_{0.2}$A$_{0.1}$
C$_2$A$_1$M$_2$	44	37	8	5	7	F$_{1.2}$S$_1$C$_{0.2}$A$_{0.1}$M$_{0.2}$
C$_2$A$_2$M$_5$	38	33	7	7	15	F$_{1.2}$S$_1$C$_{0.2}$A$_{0.2}$M$_{0.5}$

162

163 The alkali activating solution (Na$_2$O·1.65 SiO$_2$, with 65% H$_2$O) was produced by dissolving

164 sodium hydroxide pellets (>85% purity, Honeywell, Belgium) in a commercial sodium silicate

165 (Na$_2$O·3.3 SiO$_2$ with 63.5 wt% H$_2$O, Silmaco, Belgium) and deionized water. The solution

166 mixing for the aimed molar ratio was calculated using the relevant app in the online SREWay

167 platform (http://sreway.info). The activator was prepared at least 24 hours before the paste

168 preparation.

169

170 To fully focus on the effect of slag chemistry on acid resistance, only paste samples were used

171 in the present work. For the mixing, the slag to activating solution mass ratio was 0.4. During

172 mixing, the slag was mixed with the activating solution for 3 minutes using a hand mixer to

173 form a homogenous paste and was then cast into a sealed cylindrical mold with a diameter of

174 1.3 cm and height of approximately 4 cm. The paste samples were cured at ambient temperature

175 (20 °C, 50% relative humidity) for 27 days. Subsequently, they were embedded in a low-

176 density epoxy under vacuum conditions, and after 1 day, when the epoxy fully hardened, the

177 resin on the bottom surface was ground away. Hence, only the bottom surface came into contact

178 with the acid solution when samples were exposed to sulfuric acid.

179   A commercial CEM I 52.5N (PC) was used as a benchmark, and the chemical composition is

180   shown in Table 2. The paste was made with a water-to-cement ratio of 0.4 and the same mixing

181   and curing methods as for the AAM paste samples. After 28 days from casting, the paste

182   samples were immersed in 2 wt.% sulfuric acid. The H_2SO_4 solutions were replaced every

183   month over a period of 6 months to maintain the acid environment.

184   *Table 2 Chemical composition of PC (in wt %)*

	Fe_2O_3	SiO_2	CaO	Al_2O_3	MgO	SO_3	K_2O	Na_2O	Other
PC	3	20	63	5	2	3	0.6	0.3	4

185

186   After every month, the cylindrical paste samples were taken out from the used solution and the

187   corrosion depth was measured using μ-CT (Tescan UniTOM XL). The μ-CT was performed

188   with an Al filter at the focal spot. The greyscale resolution of detector is 16 bit. The condition

189   of the data collection was: X-ray power of 18 W, beam energy of 180 kV, step size of 0.2/360°.

190   Balancing the need to maximize scan area with maintaining precision led to the selection of an

191   18 μm voxel size. 1500 projections were taken with 270 ms exposure time. The reconstruction

192   of the 2D image was conducted using Datos|x software. For the calculation of the corrosion

193   depth, the measurements run in duplicate, and for each sample, at least 5 slices and 10 points

194   from the corrosion boundary to the original surface of each slice were measured. The average

195   from the depth measurements is reported hereafter as the final corrosion depth.

196

197   After 6 months, the bottom surface of the samples was stabilized by a low-density epoxy resin

198   to prevent the corroded section from dropping out during the following cutting. Afterward, the

199   stabilized cylindrical samples were cut from the middle of the longitudinal side using a low-

200   speed diamond saw. In order to study the deterioration, both the bottom-corroded layers and

201   the top intact area were analyzed.

202

203   The microstructure and the concentration of the different elements for both the corroded layers

204   and the intact fraction were measured using scanning electron microscopy (SEM) equipped

205   with Energy-dispersive X-ray spectroscopy (EDX). For this purpose, cross-sections after

206   cutting were impregnated in a low-density epoxy resin. After the hardening of the resin, the

207   surface underwent a polishing procedure using a 9 µm-diamond suspension solution, followed

208   by 3 µm and 1 µm abrasives, each applied for 5 minutes. Subsequently, a 2 nm-thick Pt coating

209   was applied to guarantee the sample was conductive. SEM (XL30, Philips) was performed at

210   an accelerating voltage of 15 kV. Elemental mapping was carried out via a field emission

211   microprobe (JXA-8530F, JEOL), and the acquired maps were processed using software

212   (TEAM software) with the eZAF algorithm for standardless quantitative analysis. The reaction

213   extent of each slag in AA-NFS prior to acid exposure was assessed through Backscattered

214   Electron (BSE) image analysis, following the procedures outlined in [36, 37]. For each AA-

215   NFS sample, a minimum of 25 micrographs were taken from different areas of the

216   microstructure at a magnification of 250x. The area fraction of unreacted NFS particles was

217   determined using Image J software. In AA-NFS, there are only two solid components:

218   unreacted slag and reaction binder. Due to the higher concentration of Fe in the unreacted slag,

219   it appears brighter in the BSE images, facilitating easy distinction and allowing for the

220   determination of the volume percentage of unreacted slag. By considering the density of the

221   slag and AA-NFS, the weight of unreacted slag can be calculated, thereby enabling the

222   evaluation of the reaction degree. Given that every NFS presents more than 95% amorphous

223   phase, except $C_2A_2M_5$, which contains only 82% amorphous phase, and considering the

224   absence of the crystal phase (olivine) involvement in the reaction process for NFS, the

225   determination of the reaction extent for $C_2A_2M_5$ in AA-$C_2A_2M_5$ was only based on the

226   amorphous phase.

227

228 The corroded layers and intact area were also milled separately until a particle size $< 0.125\ \mu m$

229 was reached for the XRD and FTIR analysis. XRD was carried out using a Bruker D2 Phaser

230 instrument. Data were collected with Cu Kα radiation of 30kV and 10mA, in a 2 theta range of

231 10-70° with a rate of 2° /min. Attenuated total reflection Fourier transform infrared (ATR-

232 FTIR) spectra were collected using a Bruker Alpha-P on the powder samples, over the range

233 of 4000-380 cm^{-1} and 32 scans per spectrum with 4 cm^{-1} resolution. The spectrum was analyzed

234 by the software Opus.

235

236 Sample AA-C$_2$A$_2$M$_5$ was characterized before and after the acid attack using solid-state ^{29}Si

237 and ^{27}Al magic angle spinning (MAS) nuclear magnetic resonance (NMR) to further examine

238 the changes in chemical arrangement after the sulfuric acid attack. The NMR spectra were

239 measured at 25 °C on a Varian Inova 500 MHz NMR spectrometer ($B_0 = 11.7\ T$). The

240 resonance frequencies of ^{29}Si and ^{27}Al were at 99.3 ppm and 130.23 ppm, respectively. A

241 single-pulse sequence was applied to all measurements. The ^{29}Si spectra were acquired using

242 a Varian 7.5 mm double air-bearing ZrO$_2$ rotor at a spinning frequency of 6 kHz. The 90 ° pulse

243 length was calibrated to 10.5 μs. The relaxation delay was set as 5 seconds for intact paste and

244 30 seconds for the corroded layers. The number of scans for C$_2$A$_2$M$_5$ – AAM before the acid

245 attack and the corroded layer are 102400 and 2048, respectively. The ^{29}Si spectra were

246 referenced to an external standard sample of tetrakis(trimethylsilyl)silane (TKS). The ^{27}Al

247 spectra were measured using a Varian 2.5 mm double air-bearing probe at a spinning frequency

248 of 20 kHz. The calibrated 90 ° pulse length was 2 μs. Relaxation delay was set as 0.5 s. The

249 number of scans is 102400 for AA-NFS before the acid attack and 10240 for the corroded layer.

250 The ^{27}Al spectra were referenced to 1M Al(NO$_3$)$_3$ solution. The deconvolution of the ^{29}Si

251 spectrum of the corroded layer was performed in FitYK software using Gaussian functions.

3. Results and discussion

3.1 Corrosion depth

Figure 1 presents a 2D slice from µ-CT images of AA-NFS after exposure to sulfuric acid for 1 month. As only the bottom surface was immersed in the sulfuric acid solution, one-direction corrosion was observed. The boundary between corroded layers and intact area is relatively flat (as indicated in the red line in Figure 1), which is helpful to obtain a reliable corrosion depth with low data scattering.

AA-NFS shows a different corrosion behavior, in comparison with cement, as appears in Figure 1. In the case of cement, a slight expansion occurs, accompanied by the presence of a white substance. The expansion is due to the formation of gypsum or ettringite, resulting from the reaction of the sulfuric acid with the calcium hydroxide and the reaction of formed gypsum with aluminate phases in the hydrated cement [38]. This expansion caused surface scaling and resulted in the degradation of cement. On the contrary, in AA-NFS samples, the formation of this layer is absent. Instead, all AA-NFS pastes were partially dissolved after exposure to sulfuric acid, yet, as suggested by Figure 2, the dissolution kinetics were not the same. The corroded depth during 6 months in sulfuric acid is plotted in Figure 2. In the investigated range, higher Al/Si has no obvious positive effect on sulfuric acid resistance. However, variations in Ca/Si and Mg/Ca ratios have a substantial impact. The degradation was notably more pronounced in the case of AA-NFS derived from precursors with lower Ca/Si, consistent with prior research [22]. Previous studies have shown that introducing additional Ca sources in AA-NFS can enhance its sulfuric acid resistance. Moreover, the replacement of Ca by Mg, for both low and high levels of replacement, negatively affected sulfuric acid resistance, although there was only a slight change for the low replacement level.
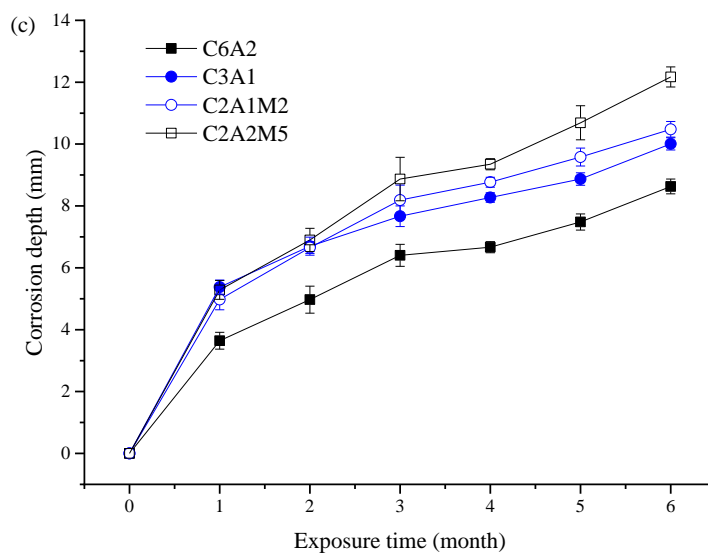
| C₆A₂ | C₆A₁ | C₃A₁ | C₂A₁ | C₂A₁M₂ | C₂A₂M₅ | Reference |

1.3 cm
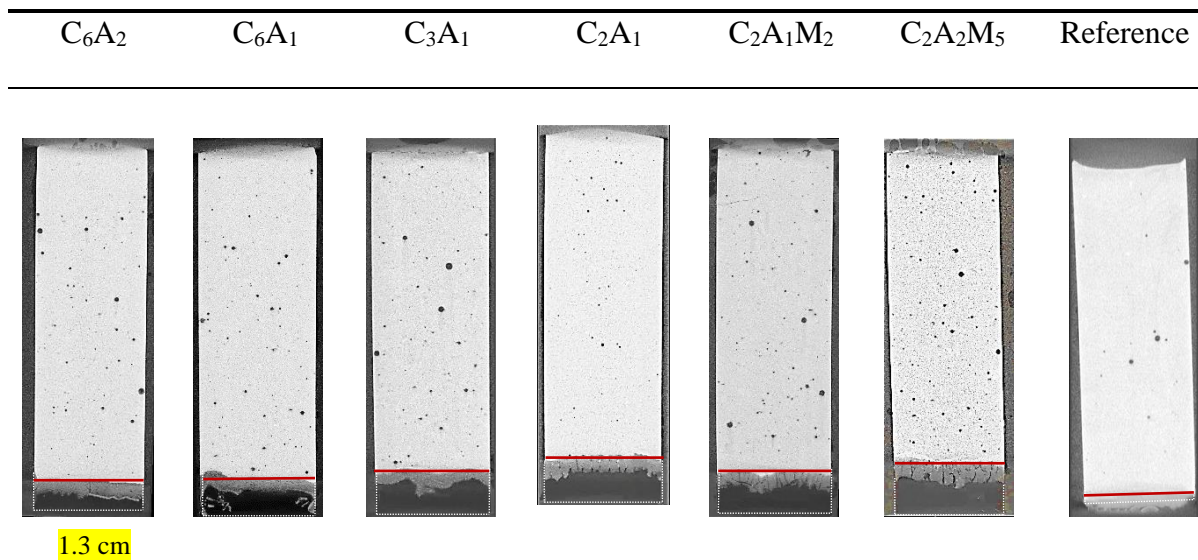
276   *Figure 1 Tomography for the samples exposed to sulfuric acid after 1 month*

277
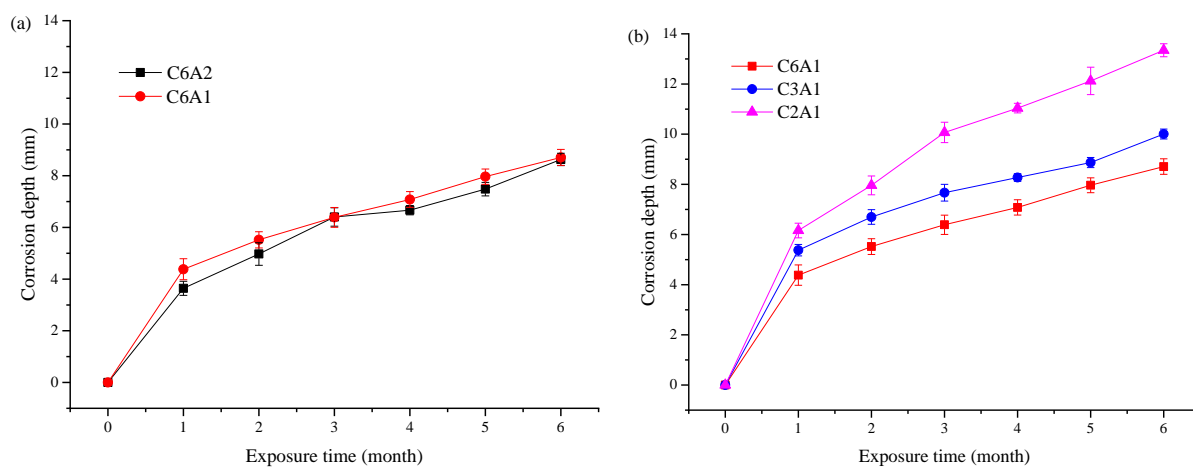
278

279

280   *Figure 2 Corrosion depth of AA-NFS samples immersed in sulfuric acid for up to 6 months (a) Al₂O₃ group (b) CaO group*
281   *(c) MgO group*

282   The evolution of physical damage was tracked using μ-CT in corresponding AA-NFS of C_6A_2

283   (which obtained the lowest corrosion depth) and C_2A_1 (which obtained the highest corrosion

284   depth) immersed in sulfuric acid for 6 months, and the results are shown in Figure 3. The 2D

285   tomography depicting degradation for the other four AA-NFS and PC can be found in

286   Appendix Figure A.2. For AA-NFS with higher Al/Si and Ca/Si (C_6A_2), the corrosion

287   happened through a denser degraded product layer, indicated by fewer cracks in the degraded

288   area. This layer could potentially act as a barrier, thereby possibly inhibiting the progress of

289   the corrosion process. Over 6 months in sulfuric acid, this layer grows thicker on the surface.

290   However, for the low Ca-system, this degraded product layer is full of cracks and quite

291   permeable. The interconnected pores or cracks provided a much easier path for the ingress of

292   the sulfuric acid toward the paste matrix and thus corrosion occurred with limited impediment.

293   From the observations here, the structure including the thickness and porosity of this degraded

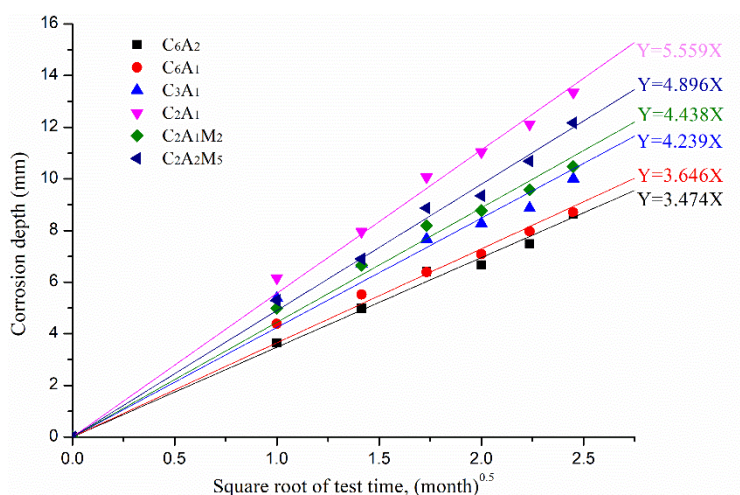294   layer could explain the different corrosion rates for different AA-NFS.
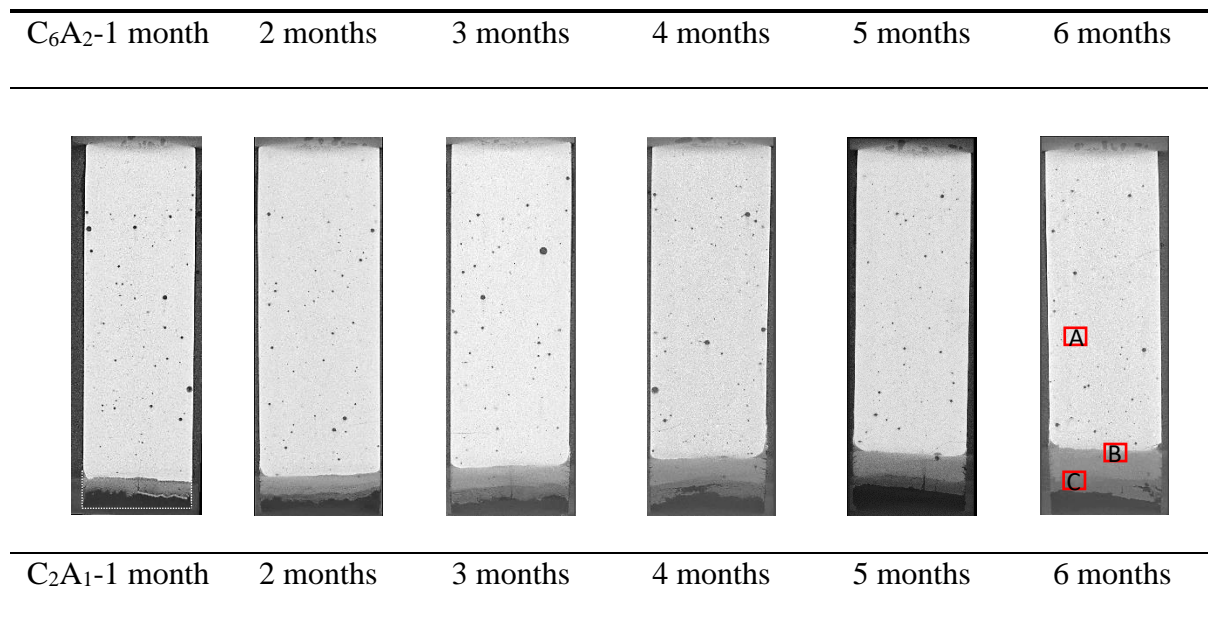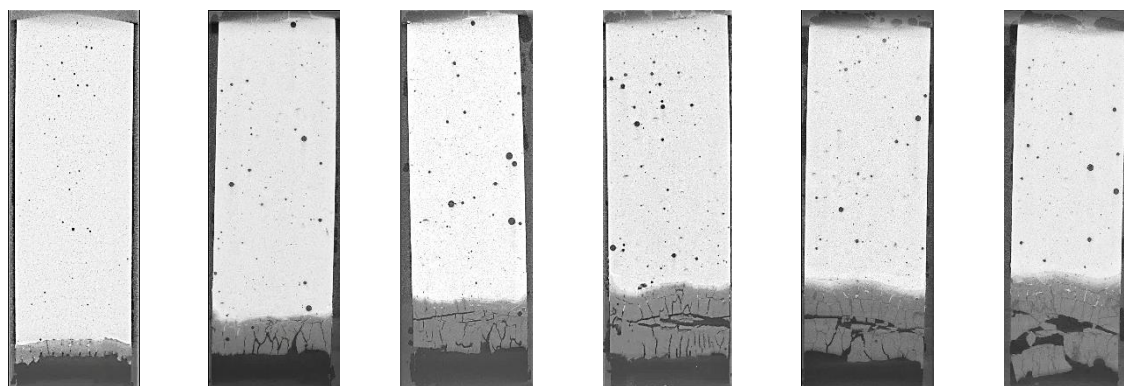
1.3 cm

Figure 4 Corrosion depth and fitted lines for AA-NFS samples immersed in sulfuric acid for 6 months

Figure 4 plots the fitting between the corroded depth and the square root of exposure time. As stated by Pavlik [16], for one-direction corrosion, the diffusion process follows a square root of time. Therefore, there is a linear function between the thickness of the corroded layers and the square root of exposure time according to the model of Fick's laws of diffusion. A linear fit was exhibited in Figure 4, which reflects that the case in this study is a diffusion-controlled model rather than a reaction-controlled one. This is in line with the findings from previous

308 work [31]. Although the diffusion control model remains valid, discrepancies are observed in

309 the fitting data initially lying above the fitting line and later below it. Another study introduces

310 a novel model for AA-NFS in sulfuric acid solution [39]. Given that Fe^{3+} within the AA-NFS

311 exists in a silicate network, the dissolution of Fe^{3+} serves as an indicator of framework

312 deterioration. Thus, monitoring the leaching of Fe^{3+} from the AA-NFS silicate network serves

313 as a measure of framework degradation. This enables the evaluation of degradation by tracking

314 changes in Fe^{3+} concentration over time in the acid solution using NMR. Results indicate that

315 chemical reactions control leaching in the first few hours, followed by diffusion over time. The

316 precision of this in-situ test may account for the observed deviation. Despite the fitting data

317 spanning 6 months, the dominance of diffusion control largely persists, given the prolonged

318 exposure time. The slope of the fitted line can serve as a key parameter for assessing the

319 potential corrosion degree in AA-NFS.

320

321 In a previous study [36], a dissolution test was conducted in which both NFS C_6A_2 and AA-

322 C_6A_2 were immersed in sulfuric acid. The results indicated that unreacted slag particles are

323 more susceptible to sulfuric acid damage than the reacted binder in AA-C_6A_2. This observation

324 suggests that the extent of the NFS reaction in AA-NFS may ~~have a significant influence~~

325 ~~on~~influence the corrosion degree of AA-NFS in sulfuric acid. Figure 5 presents a plot of the

326 reaction extent of AA-NFS against the corrosion degree which is indicated by the slope in

327 Figure 4, with error bars indicating the variation in the BSE images used for reaction extent

328 evaluation. This plot ~~clearly~~ demonstrates a ~~strong~~ negative correlation between the reaction

329 extent and corrosion degree, which shows that a higher reaction extent of slag corresponds to

330 a lower corrosion degree. This correlation provides an explanation for the varying degradation

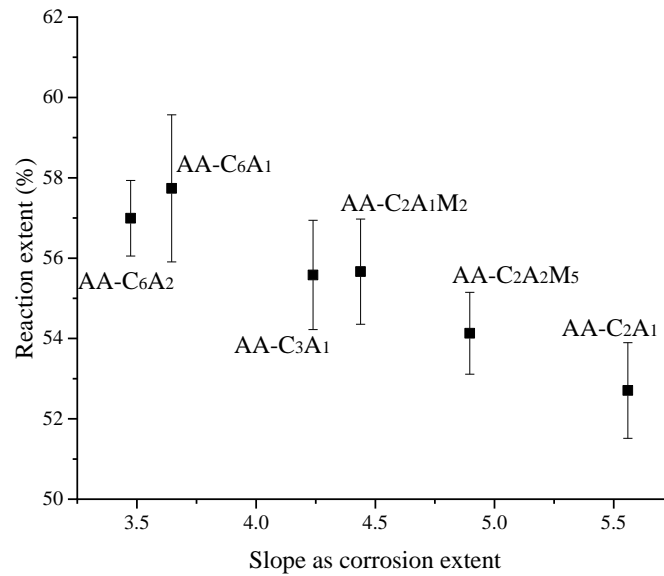331 degree observed in different AA-NFS when exposed to sulfuric acid.

332

333

334

3.2 Microstructure of the corroded samples

336 ~~As all the AA-NFS present similar degradation mechanisms, t~~The microstructures of AA-C$_6$A$_2$

337 and AA-C$_2$A$_2$M$_5$ were taken as examples for SEM imaging (Figure 6). For the intact area

338 (delineated in Zone A of Figure 3), as seen in Figure 6a (C$_6$A$_2$) and 6b (C$_2$A$_2$M$_5$), the

339 morphology of AA-NFS pastes exhibits a homogenous reacted binder with unreacted slag

340 particles embedded inside. There are visible cracks, which formed most likely due to the drying

341 shrinkage or the vacuum process in the SEM sample preparation.

342

343 The microstructure of the transition between intact and corroded layers (delineated in Zone B

344 of Figure 3) is shown in Figures 6c and 6d. In the corroded layers, gypsum could be detected,

345 which was also identified by XRD (to be discussed in the following 3.2 XRD session). There

346 are many sublayers observed in the corroded layers of AA-C$_6$A$_2$, separated by gypsum

347 precipitate as evidenced by the SEM images. The prevailing reason for this is most likely that

348 the diffusion process of sulfuric acid penetrating the paste matrix over time resulted in a gradual

349 deterioration [30] and the paste samples were split into pieces with neo-forming gypsum filling

350   interspaces. Some researchers have stated that gypsum clogs pores and could provide a

351   protective effect inhibiting the total process of deterioration [29]. From the comparison of

352   Figure 6c and 6d, more gypsum was observed for the C_6A_2-NFS with higher Ca contents. For

353   AA-$C_2A_2M_5$, much less gypsum was observed and a corroded structure with big cracks was

354   noticed. Hence, a decreased corroded depth with a higher Ca concentration was observed in

355   Figure 2. This could be the reason for the denser corroded layers of the AA-NFS system with

356   higher Ca concentration, and this also explains why the replacement of Ca by Mg showed lower

357   resistance to the sulfuric acid attack in this work. The zoomed-in microstructure of the corroded

358   area is presented in Figures 6e and 6f. From the comparison of the intact area and corroded

359   area, it can be noticed that the unreacted slags appear to undergo a greater degree of degradation,

360   which is in agreement with the diffusion test results [36], where the slag exhibited a tendency

361   to dissolve more easily and rapidly than the reacted binder.

362
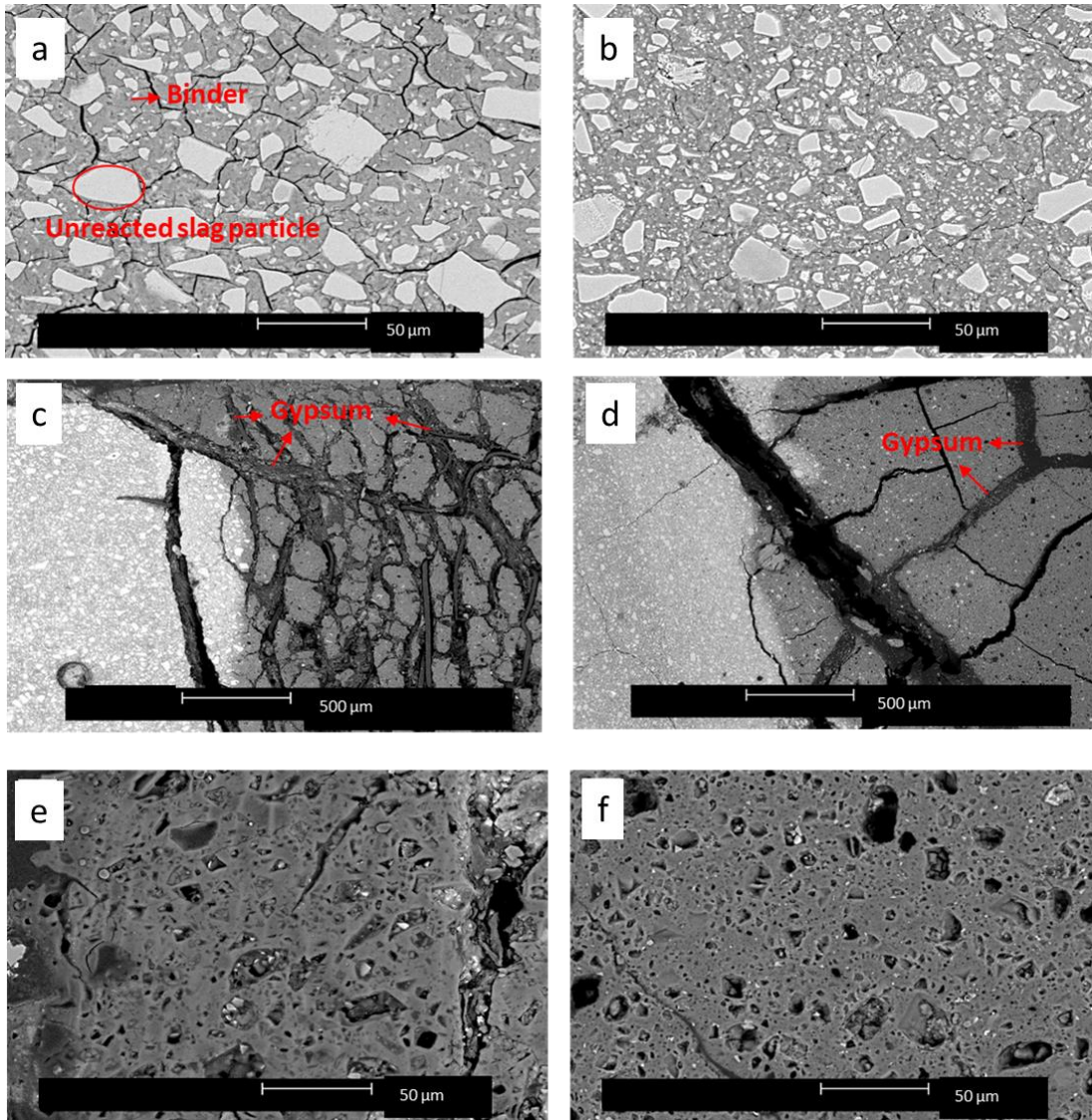
Figure 6 SEM analysis of AA-C_6A_2 and AA-$C_2A_2M_5$ after the exposure to sulfuric acid: (a) intact area of AA- C_6A_2; (b) intact area of AA-$C_2A_2M_5$; (c) transition area of AA- C_6A_2; (d) transition area of AA-$C_2A_2M_5$; (e) corroded area of AA- C_6A_2, and (f) corroded area of AA-$C_2A_2M_5$

A zoomed-in view of the transition zone (delineated in Zone B of Figure 3), for AA-$C_2A_2M_5$ after the sulfuric acid attack characterized using EDX is shown in Figure 7. From the elemental distribution, the formation of gypsum is visible. The dissolution of slag and binder led to the oversaturation of the interstitial solution with respect to calcium sulfate phases [10], and led to the formation of gypsum as a consequence.
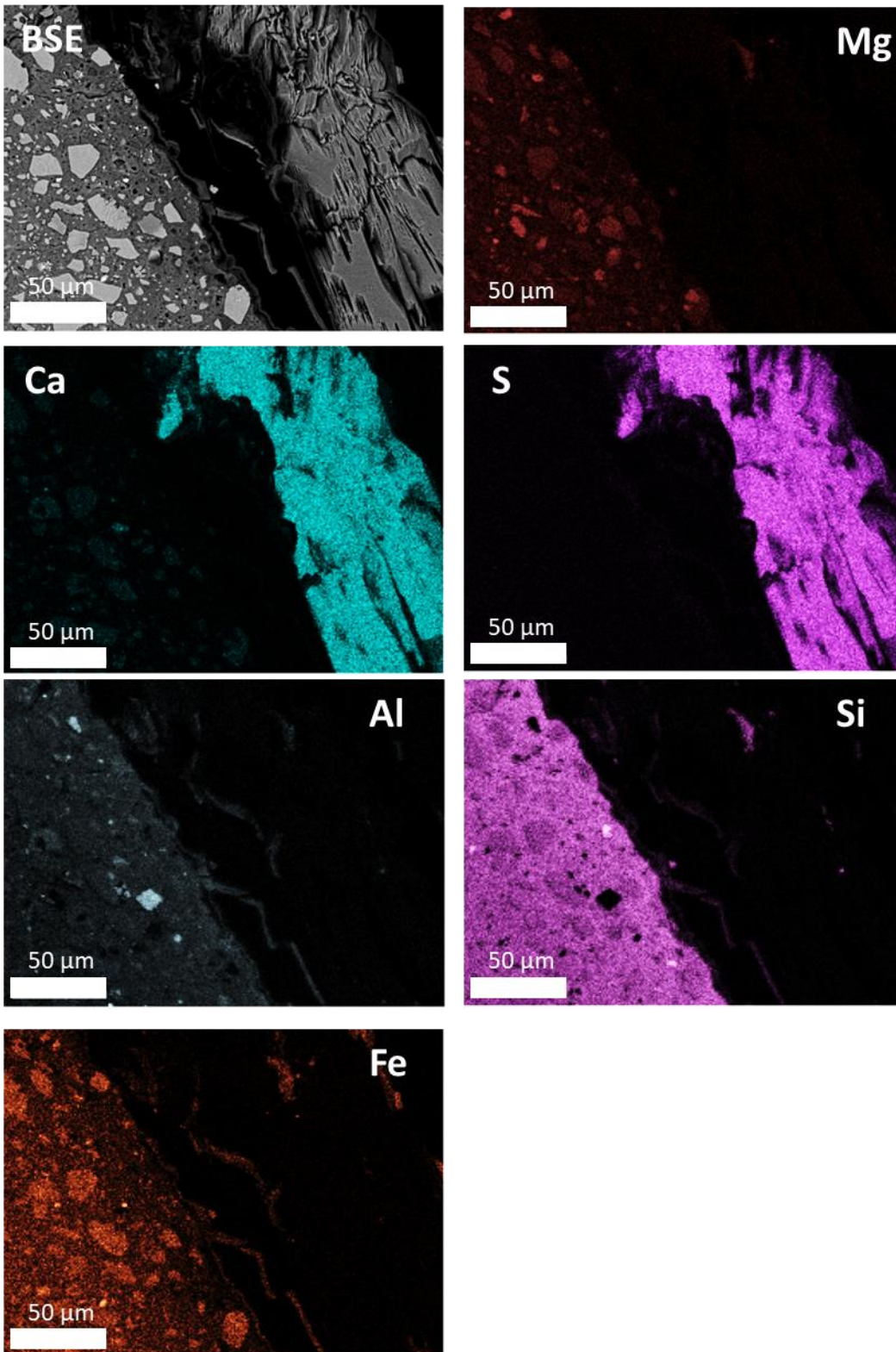
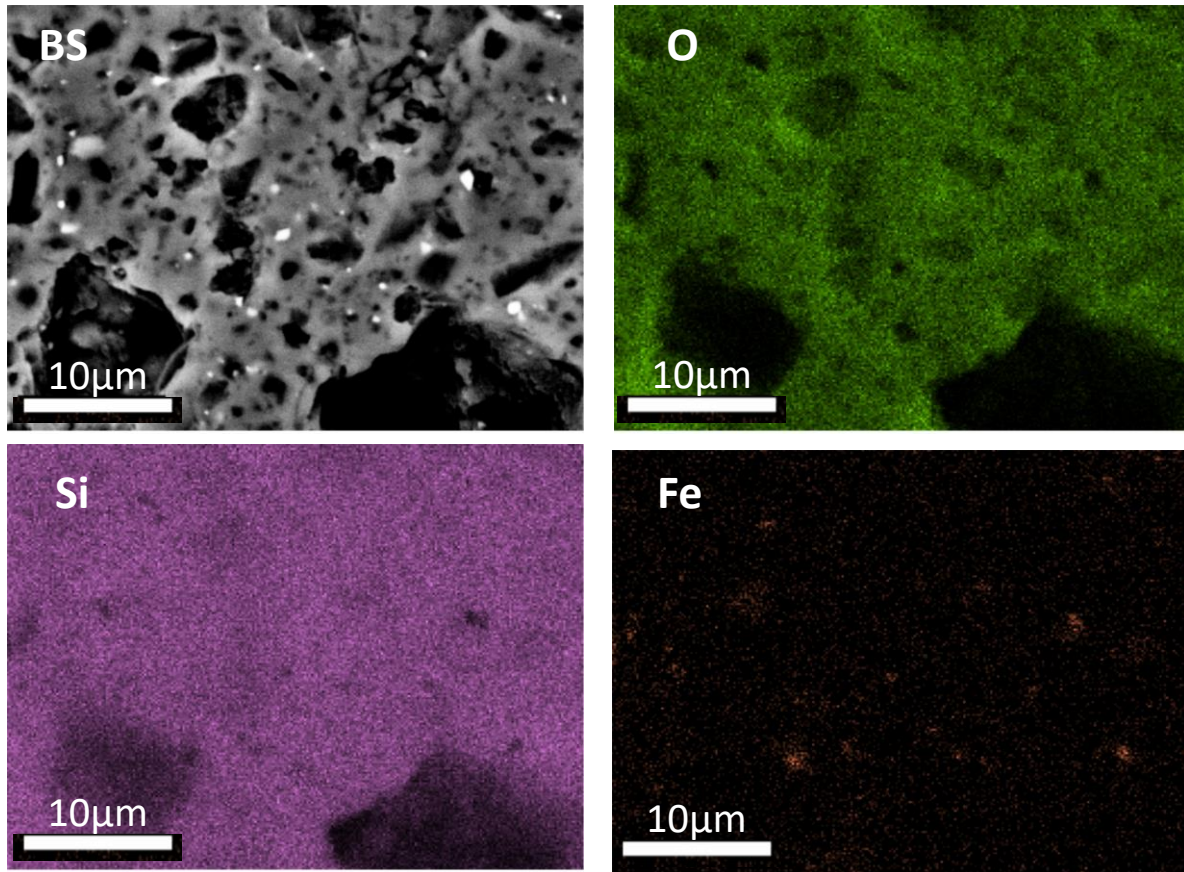*Figure 7 Mineral phase distribution of the transition zone of AA-$C_2A_2M_5$ by EDX measurement*

The elemental mapping of the corroded front (delineated in Zone C of Figure 3), for AA-$C_2A_2M_5$ is presented in Figure 8. In this area, no unreacted slag was found. A complete

376 transformation was noted as only a depleted amorphous silica gel network was formed from

377 the original reaction product. This was also indicated in section 3.4 FTIR analysis and

378 indirectly reveals the leaching out of the ions (Na^+, Ca^{2+}, Mg^{2+}, Al^{3+} and Fe^{x+}). Special attention

379 should be given to the role of Fe in the AA-NFS system. As Fe could be in different valence

380 states, Fe^{3+} was suggested to participate in the silicate network similar to Al, while Fe^{2+} is

381 assumed to aggregate and participate in trioctahedral layers [5, 40]. Because the silica gel is

382 the main residual structure, this suggested both Fe^{3+} and Fe^{2+} in the structure did not resist the

383 sulfuric acid attack.

384

385 It is interesting to notice that both Si and Al play the network-forming role but mostly silica is

386 left in the structure after acid attack. There are two possible reasons. One is that during acid

387 exposure, at the early stage, Al and Si in AA-NFS dissolved congruently. At a later point, this

388 activity shifted to the preferential Al dissolution process, resulting in an amorphous Si-rich gel

389 left [41]. In the acid environment, it is possible that Al ions were absent as it has a high

390 solubility in low pH [42]. The other explanation originally suggested for the formation of silica

391 gel in the system of alkali-activated GGBFS/fly ash, proposes that a large quantity of silicic

392 acid was released because of the acid attack, which triggered the precipitation of the Si gel [43].

393 Meanwhile, the dissolved Al ions could interact with the silicic acid and the resulting reaction

394 product could retard the network depolymerization [44]. Hence, the precipitation of Si gel

395 would be ongoing until the end of the experiment [43, 45], and many thin layers rich in Al and

396 Si would be detected in SEM-EDX analysis [46]. Nevertheless, as there are no such rich in

397 both Al and Si layers detected, the first explanation appears to be more persuasive. To confirm

398 this, additional dedicated research (e.g. (in-situ) dissolution tests) is required to elucidate the

399 dissolution mechanisms of Al and Si.

Figure 8 Mineral phase distribution image of the corroded layers of AA-$C_2A_2M_5$ by EDX measurement

The degradation observed in Figures 6-8 involves one-dimensional attack, occurring vertically within the samples, as acid gradually penetrates the inside matrix. To further examine microstructural changes, an etching test was conducted. However, after 2 hours of exposure to sulfuric acid, the surface becomes uneven, which compromises the quality of measurements and introduces the potential for errors in the analysis. Thus, the results of the etching test are presented in Appendix Figure A.4.

3.3 XRD analysis

The XRD patterns for slag precursors, intact area and corroded layers of AA-NFS after the sulfuric acid attack are shown in Figure 9. All slags are amorphous glasses, except for slag $C_2A_2M_5$, which is predominantly amorphous but features also a minor crystalline phase of olivine and hercynite. The XRD patterns of AA-NFS in the intact area are similar to the original

414   slag, with a big hump centered at approximately 32° 2Θ arising from the amorphous nature of

415   unreacted slag and reacted binder. The reflections of olivine and hercynite remain unchanged

416   in the AA-$C_2A_2M_5$, which indicates that these crystalline phases are inert in the alkaline

417   solution [19].

418

419   All samples underwent significant changes after the sulfuric acid attack as the XRD patterns of

420   corroded layers are totally different from the intact area. Instead of a hump between 22-38°,

421   there is a broad hump centered at around 22°. This confirms the complete loss of unreacted

422   slag and reacted binder and the formation of the amorphous silica gel [13, 47], consistent with

423   the observations in SEM images. The formation of gypsum and the loss of unreacted slag and

424   binder are consistent with the literature [30], where XRD patterns of alkali-activated GGBFS

425   exposed to 1-5% sulfuric acid for 28 days were examined. Along with this hump, the

426   characteristic diffraction peaks of gypsum were observed. A comparison of the gypsum peak

427   intensities indicates that the more Ca was present in the system, the more gypsum was formed

428   after the sulfuric acid attack.
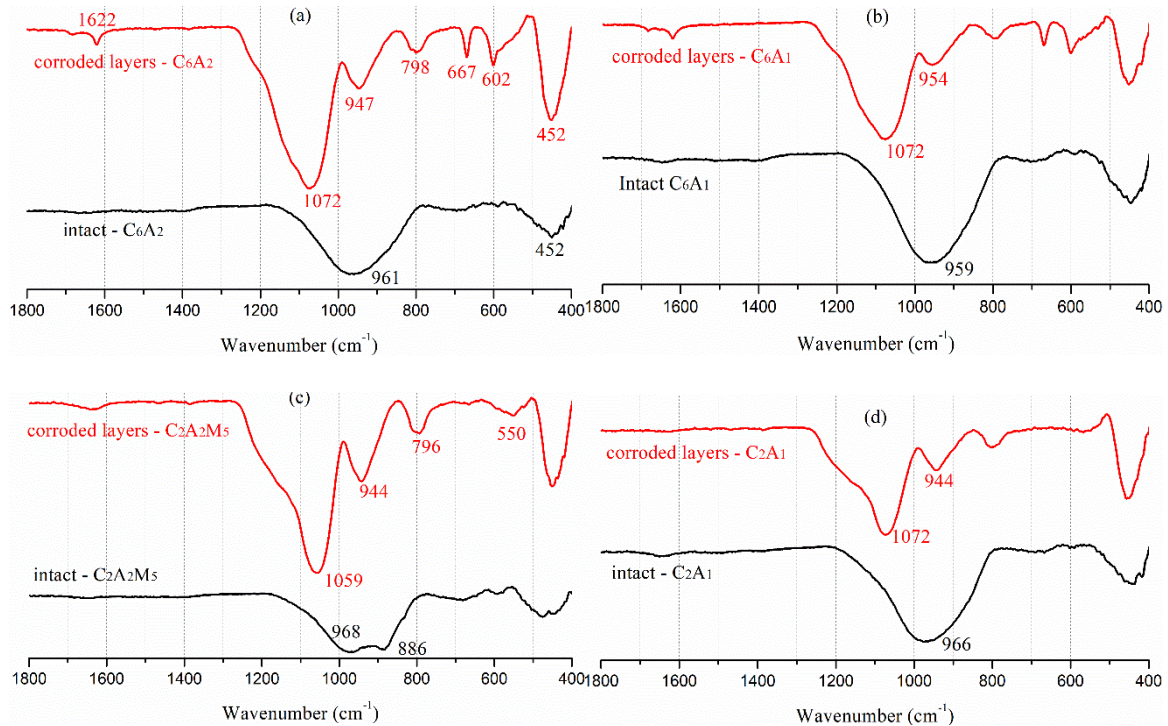
429
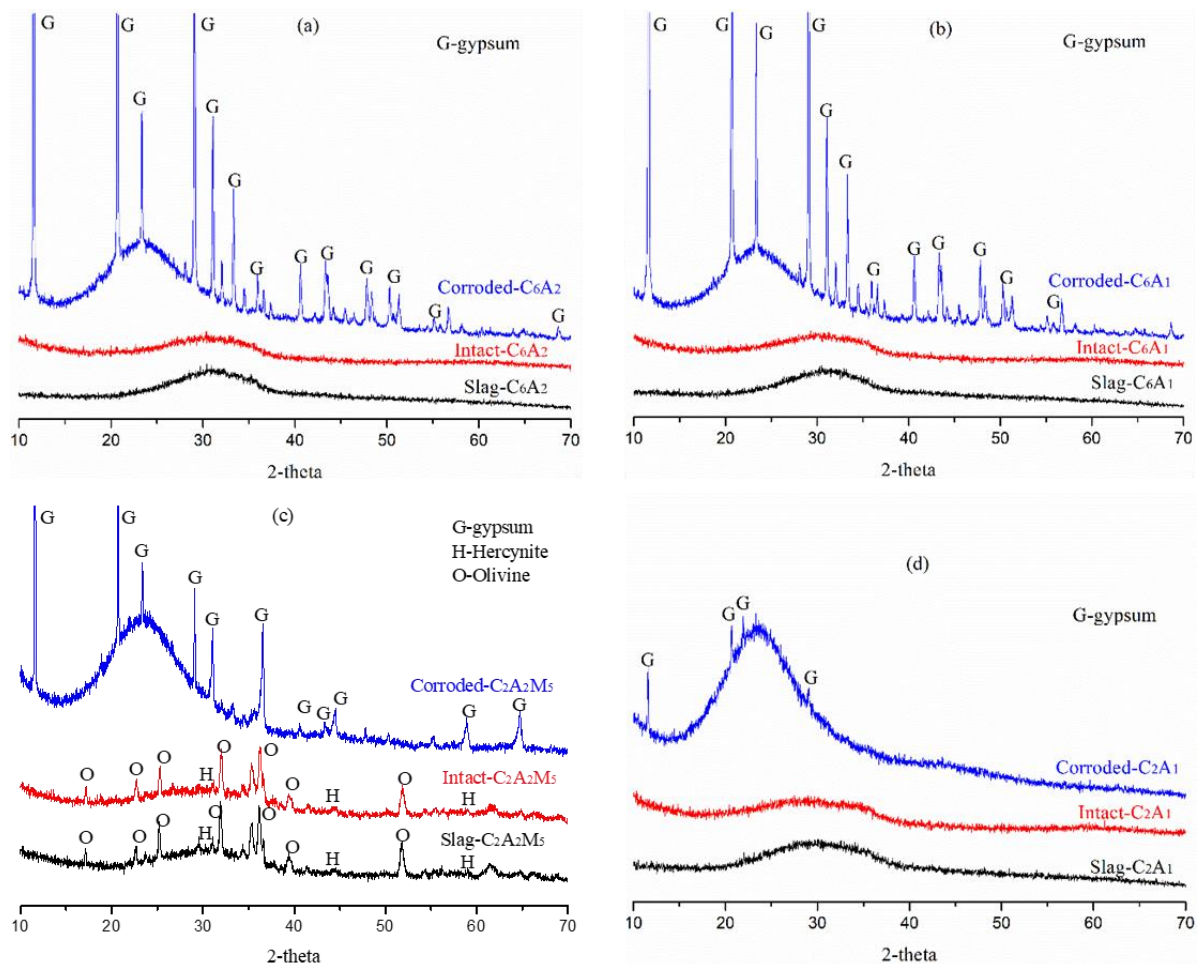
Figure 9 XRD patterns of the AA-NFS exposed to sulfuric acid for the intact area and corroded layers

3.4 FTIR

Figure 10 exhibits the FTIR spectra of the intact area and corroded layers of AA-NFS after exposure to the sulfuric acid solution. To focus on the network evolution, spectra in a wavenumber region of 1800-400 cm^{-1} are presented. For the intact area, the spectra are dominated by a broadband for all the samples. The vibration at approximately 960 cm^{-1} is attributed to the asymmetrical Si-O-T (T= Fe, Al, or Si) stretching bond [48]. Additionally, this broadband is sensitive to the T-Si ratio and more Al or Fe atoms could shift the wavenumber to a lower value [49] due to the widening of the Si-O-T distance compared to the Si-O-Si bond [7]. Another main band detected at around 450 cm^{-1} corresponds to the Si-O asymmetric bending bond [50]. A band at 1400 cm^{-1} with minor intensity, assigned to the C-O vibrations, indicates the presence of minor contents of carbonates [48]. The FTIR spectra for the intact

443 area of AA-NFS are similar, except there is a small band at approximately 886 cm^{-1} in AA-

444 C$_2$A$_2$M$_5$, which is associated with the crystalline phases in the unreacted slag.

445

450 After sulfuric acid exposure, all AA-NFS show similar spectra. The small band at 886 cm^{-1} for

451 AA-C$_2$A$_2$M$_5$ is not detected anymore, suggesting these crystalline phases in C$_2$A$_2$M$_5$ do not

452 exist after sulfuric acid attack. The main band of Si-O-T significantly shifts to a higher

453 wavenumber around 1059 cm^{-1} and becomes sharper, suggesting the large extent of leaching

454 out of Al, Ca, Mg and Fe from the polymer as well as the incorporation of Si into the polymer,

455 leading to a highly polymerized structure. In addition, it shows the highly amorphous character

456 of the corroded layers as pure silica glass, which has a band centered around 1080 cm^{-1} [51].

457 This is consistent with the observed silica gel in the SEM-EDX and XRD results conducted in

458 section 3.2. Moreover, the main band overlaps with the S-O stretching mode of gypsum at

459 around 1115 cm^{-1} [13]. Bands at around 947 cm^{-1} arising from the Si-O stretching vibration of

460 Si-OH groups [52] were observed for all the AA-NFS, corresponding to a slight shoulder

461   around 850 cm^{-1} for the intact area. The appearance of new sharp bands at 1622, 798, 667 and

462   602 cm^{-1} indicates the presence of gypsum [53]. The intensity of these bands is much lower for

463   low Ca-AA-NFS. There is no significant change in the bending modes around 450 cm^{-1} as it is

464   not sensitive to the Al, Ca, Mg, and Fe substitution [49]. These FTIR spectra combined with

465   the XRD patterns reveal the highly polymerized amorphous silica gel is formed after the

466   sulfuric acid attack [13], which is consistent with the SEM-EDX analysis.

467   3.5 Solid-state NMR results

468   3.5.1 ^{27}Al MAS NMR

469   Figure 11 shows the ^{27}Al MAS NMR spectra of the AA-C$_2$A$_2$M$_5$ sample before and after the

470   6-month sulfuric acid attack. The spectrum of AA-C$_2$A$_2$M$_5$ exhibits pronounced intensity of

471   sidebands symmetrically distributed on both sides of the central peaks. However, the amplitude

472   of sidebands in the sample after the acid attack reduced drastically, which indicates that most

473   of the paramagnetic ions (Fe in our case) have been leached out from the original sample. The

474   spectrum also shows higher resolution after the acid attack. The unpaired electrons in the Fe

475   ions can interact with the nearby nuclear spins through dipolar coupling, which is hardly

476   removed by the MAS. The signal is thus separated and refocused at the spinning frequency.

477   The intense electron-nuclear dipolar interaction also causes the line to broaden, resulting in

478   lower spectral resolution. Therefore, the sidebands intensity and the spectral resolution can be

479   used as indicators of the concentration of paramagnetic ions.

480

481   Focusing on the central peaks (Figure 11b), the intact AA-C$_2$A$_2$M$_5$ is identified by one

482   pronounced broad region centered at 60.5 ppm and a small hump at 14.0 ppm, which

483   correspond to Al in tetrahedral (Al(IV)) and octahedral (Al(VI)) sites, respectively. The

484   resonance at 60.5 ppm denotes Al in a q^4(4Si) environment, where the Al(IV) coordinates with

485   4 tetrahedral silicon through oxygen bridge sites [54]. The tetrahedral Al is attributed to the Al

486   in the siliceous network. The octahedral Al at 14 ppm is similar to that in hydrated aluminates,

487   such as the AFt group [55]. However, this octahedral Al might be associated with layered

488   double hydroxides or phyllosilicate-like phases, which were previously found in Fe-rich AAMs

489   [50, 56] or, the most likely scenario, this is indicative of undissolved slag in the AA-NFS paste.

490   Interestingly, this peak is also present after sulfuric acid exposure, meaning that this phase is

491   not attacked by sulfuric acid or that the product of sulfuric acid attack has the same local

492   environment of Al. However, due to the impact of Fe ions, it would be problematic to just

493   directly compare the ^{27}Al spectra intensity before and after the acid attack.

494

495   Upon 6 months of exposure to the sulfuric acid, the Al(IV) resonance shifts from 60.5 ppm to

496   53.1 ppm, suggesting that Al(IV) is still in the q^4(4Si) environment. This can be assigned to

497   the tetrahedral Al coordination in the residual AA-$C_2A_2M_5$ or in the freshly formed gel. The

498   shift in Al(IV) resonance can be attributed to the replacement of charge-balancing cations or

499   network modifiers cations by H^+ from the acid. A narrow resonance at 0 ppm is detected, which

500   can be assigned to Al(VI) in well-defined octahedral coordination. It originates from the

501   formation of amorphous alumina hydrates under the acid attack [57]. The dealumination and

502   the removal of charge-balancing cations and network modifiers cations from the AA-NFS

503   network can lead to the decomposition of the initial phase in the AA-NFS. The loss of

504   aluminum from the tetrahedral framework is consistent with the FTIR results, which will be

505   further confirmed by the ^{29}Si NMR in the next section.

506

507
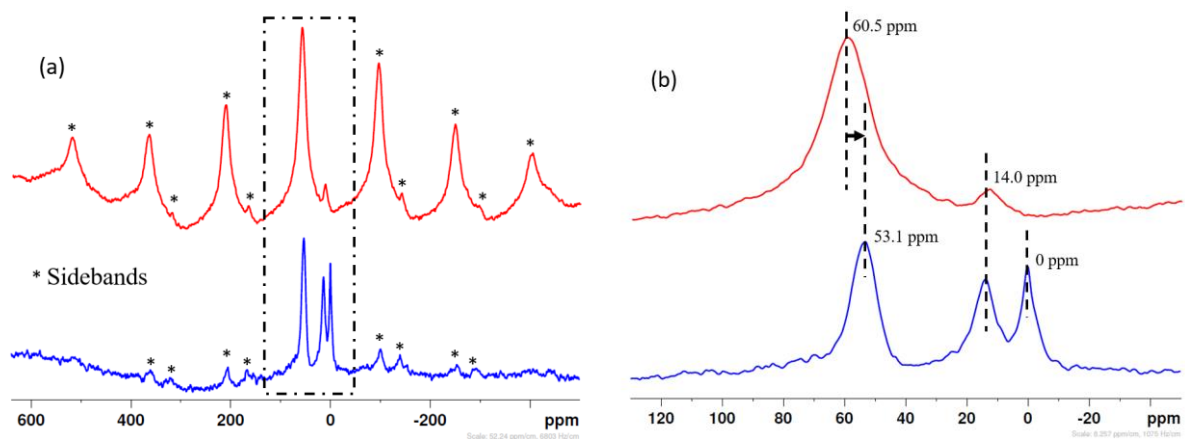
Figure 11 ^{27}Al MAS NMR spectra of C2A2M5-AAM before (red) and after (blue) 6-month sulfuric acid attack: (a) full spectra, and (b) central peaks. Sidebands are marked with *.

3.5.2 ^{29}Si MAS NMR

The ^{29}Si MAS NMR spectra of AA-C$_2$A$_2$M$_5$ before and after exposure to sulfuric acid for 6 months are shown in Figure 12. Due to the effect of Fe ions, an extremely broad resonance from -58 ppm to -135 ppm is observed in the sample before the acid attack, resulting in a low resolution. This broad line covers a very wide frequency range, including Q^0 to Q^4, thus we could not exclude the possibility of any species. In addition, Fe-O-Si bonds might not be detected by the NMR because they relax too fast before detection. Also, the hyperfine interaction between unpaired electrons and the nucleus might shift the resonance (known as fermi and pseudo-contact shifting). These uncertainties bring difficulties to quantitative analysis (deconvolution) and further qualitative assignments. Nevertheless, it can be observed that the dominant ^{29}Si resonance is centered at -82 ppm, which belongs to the Q^2 group sites. After the acid attack, the spectrum becomes well resolved due to iron removal. The shift in ^{29}Si resonance reveals extensive changes in microstructure. The main signals now occur at chemical shifts of -100 ppm and -110 ppm corresponding to silicate tetrahedra in Q^3 and Q^4 environments, suggesting the generation of more cross-linked gels after the acid attack.

527　Deconvolution was only applied on the spectra of samples after the acid attack, to better

528　understand the gel structure via ^{29}Si MAS NMR. Figure 13 exhibits the fitting peaks, simulating

529　curves and experimental data. The peak positions were referenced from the literature [58], in

530　which a similar line shape was observed in a cement sample stored in HCl at pH 2 for 28 days.

531　The ^{29}Si spectrum can be deconvoluted into eight peaks and Si can be distributed into different

532　sites (Table 3). The percentage of tetrahedral silicate in these sites, derived from the

533　deconvolution, can also be found in Table 3. Using the integral of the signal intensities, one

534　can calculate the Si/Al ratio in the framework based on Engelhardt's formula for N-A-S-H [59]

535　and the formula for C-A-S-H [60]. The Si/Al ratio calculated for silicate gel is about 41, which

536　is much higher than the initial ratio of around 2.5. Considering most of the aluminum in the

537　AAM is coordinated with Si in the framework according to the ^{27}Al spectrum, the designed

538　Si/Al ratio can be considered to be the ratio in the AAM framework. The Si/Al ratio in the

539　framework increased over 16 times after the acid attack, which demonstrates the dealumination

540　during acid exposure. These findings are consistent with the results from SEM and FTIR.

541　*Table 3 Results from the deconvolution of $C_2A_2M_5$ - AAM after exposure to sulfuric acid for 6 months*

site	Positions (ppm)	Distribution of Si (%)
Q^4	-119, -110, and -107	55.7
$Q^4(1Al)$	-104	5.7
Q^3	-101	28.7
$Q^3(1Al)$	-96	5.0
Q^2	-92	4.7
$Q^2(1Al)$	-86	0.2

542

543　Apart from the small amounts of aluminum in the framework, the percentage of silicate species

544　and their resonances are consistent with those in the silica gel prepared at acid conditions (pH

545　4) [61]. As demonstrated by XRD and SEM, the precipitation of gypsum depleted the calcium

546　in AA-NFM. Thus in the silica gel, most of the Q^3 sites are not calcium modified but attribute

547　to single silanol groups of Si(OSi)$_3$OH. Similarly, the Q^2 sites are probably geminate silanol

548　groups Si(OSi)$_2$(OH)$_2$. Overall, the NMR results confirmed that silica gel with a more cross-

549 linked structure tends to form after a long-term sulfuric acid attack, accompanied by the

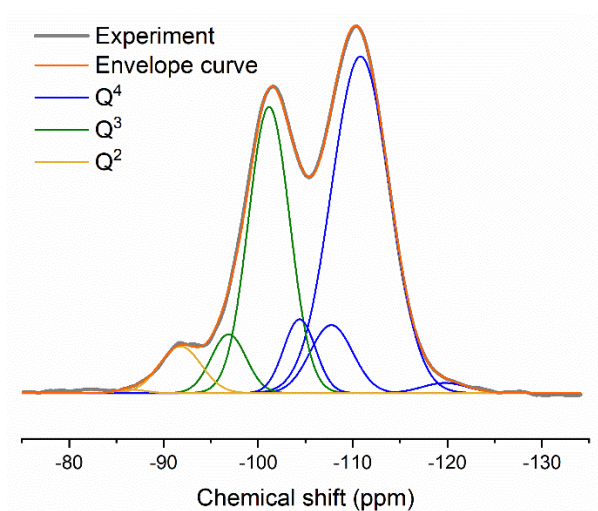550 leaching out of cations such as Fe^{3+} (Fe^{2+}), Na^+, Ca^{2+}, and Al^{3+} from the AAM.
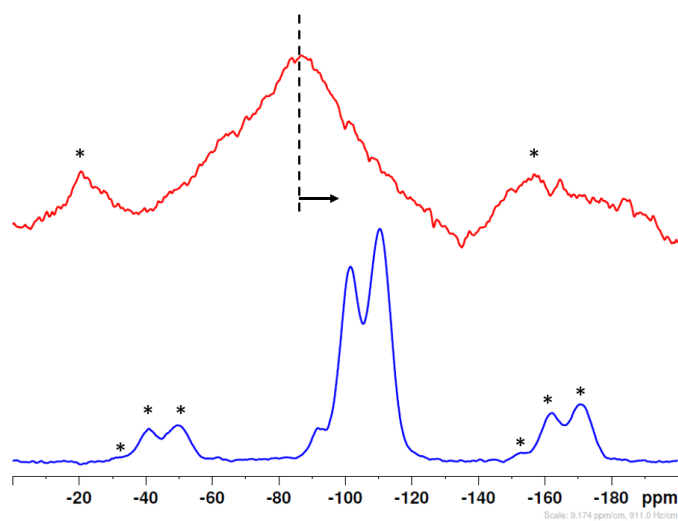
551

552 *Figure 12 ^{29}Si MAS NMR spectra of C$_2$A$_2$M$_5$-AAM before (red) and after (blue) 6-month sulfuric acid attack. Sidebands are*

553 *marked with *.*

555 *Figure 13 Deconvolution of ^{29}Si spectrum of the sample after a 6-month acid attack*

556 ## 3.6 Degradation mechanism

557 The degradation process of AA-NFA in sulfuric acid significantly differs from that of PC.

558 When exposed to sulfuric acid, the primary structural components dissolve. The essential

559 charge-balancing cations or network modifiers cations (such as Na^+, Ca^{2+}, Fe^{2+}, and Mg^{2+})

560 dissolve in the acid and also the Al^{3+} and Fe^{3+} leached out from the tetrahedral framework. This

561 dissolution leaves behind a more cross-linked silica gel as the new predominant structural

562   component, as indicated by SEM, XRD, FTIR and NMR results. Furthermore, the dissolved

563   Ca^{2+} ions react with SO^{4-} ions within the sulfuric acid solution, leading to the formation of

564   gypsum in the corroded region. This gypsum could clog pores, in turn, offering an additional

565   protective barrier for AA-NFS against sulfuric acid. In addition, the degradation of AA-NFS

566   in sulfuric acid can be described as a diffusion-controlled process. A simplified representation

567   of this degradation mechanism is provided in Figure 14 for reference.
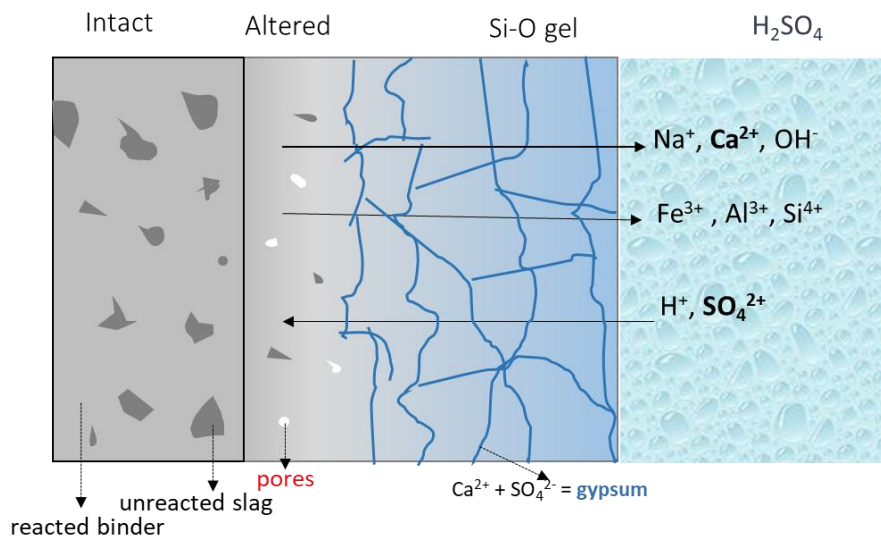
568

569   *Figure 14 Schematic diagram of the deterioration mechanism of AA-NFS in sulfuric acid*

570   The chemistry of NFS plays an important role in determining its resistance to sulfuric acid

571   corrosion. Firstly, variations in slag chemistry result in different reaction extent of NFS in AA-

572   NFS, and this reaction extent is closely associated with the extent of degradation. Secondly,

573   the structure of the degraded areas differs depending on the NFS chemistry. In particular, AA-

574   NFS with a higher Ca/Si ratio exhibit less fractured degradation areas as visually observed in

575   μCT, which inhibits the progress of the corrosion process. This can be attributed to the fact that

576   in AA-NFS systems with higher Ca/Si ratios, the intact regions are less porous [62], and on top

577   of that, the increased Ca/Si ratio increases the formation of gypsum, which effectively blocks

578   the pores. It's important to note that while this enhanced gypsum formation has a beneficial

579 effect, it is not without limits. Excessive gypsum expansion can lead to spalling, which in turn

580 may contribute to degradation, as in the cases of cement or AA-GGBFS.

581

582 The replacement of Ca by Mg has an adverse impact on the resistance to sulfuric acid corrosion.

583 Firstly, as the degradation process is diffusion-controlled, the replacement of the CaO by MgO

584 leads to higher porosity from the results of MIP [62]. As a result, it is expected that the

585 increased porosity of the AA-NFS system with MgO would result in a faster diffusion and thus

586 reduced corrosion resistance. Secondly, the replacement of Ca with Mg leads to a reduced

587 formation of gypsum, which results in less effective pore-clogging. Lastly, the replacement of

588 Ca by Mg in NFS leads to a lower reaction extent of NFS in AA-NFS. Since unreacted slag

589 particles are more vulnerable to sulfuric acid, the reduced reaction extent of AA-NFS with the

590 replacement of Ca by Mg contributes to higher degradation.

591

592 In our study, we have investigated the degradation mechanism of AA-NFS. However, it's

593 important to note that in real-world scenarios, the concentration of acid may vary, which could

594 impact the degradation process. Therefore, further studies should explore the effects of

595 different acid concentrations to provide a more comprehensive understanding. Additionally, in

596 this work, CEM I 52.5 is used as a reference material to highlight the significant differences in

597 attack mechanisms between AA-NFS and traditional cement. However, we acknowledge that

598 using sulfate-resistant (SR) Portland cement would be more appropriate, especially considering

599 its relevance to sulfate-rich environments. Furthermore, it is important to include other

600 evaluation parameters such as strength in assessing the real performance of AA-NFS. Currently,

601 no single parameter can fully evaluate the performance of AA-NFS in sulfuric acid solution.

602 Therefore, incorporating more parameters will provide a more comprehensive understanding

603 of its behavior under these conditions.

4. Conclusion

While Fe-rich metallurgical slag has already proved to be successfully applied in alkali activation, the long-term durability performance of these novel AAM is still not clear. This work explored the degradation mechanisms of AA-NFS with varying Al/Si, Ca/Si, and Mg/Ca, after exposure to sulfuric acid attack for up to 6 months. Corrosion depth, measured by μ-CT, was applied as the indicator of deterioration degree after the acid attack.

The results revealed that the slag chemistry has a significant effect on the extent of sulfuric acid attack of the AA-NFS. In the investigated range of chemical compositions, higher Al/Si had no obvious positive effect on the sulfuric acid resistance, while the replacement of Ca by Mg negatively affected the performance. Additionally, the acid resistance increased with increasing Ca/Si, which thus appeared to be crucial for sulfuric acid resistance for this novel low-Ca and high-Fe system of AA-NFS. The importance of Ca content can be related to the formation of gypsum after acid attack. As a diffusion-controlled process, which is confirmed by the development of corrosion depth, the presence of gypsum clogs pores and hinders further diffusion, leading to a lower corrosion rate. By SEM-EDX, XRD, FTIR and NMR analysis, it was revealed that after the sulfuric acid attack, ions (Na^+, Ca^{2+}, Fe^{x+}, Mg^{2+} and Al^{3+}) leach out. Al in both tetrahedral and octahedral coordination is detected because of dealumination during acid exposure. After the long-term sulfuric acid attack, the main binder and unreacted slag were completely disintegrated whereas extensive precipitation of gypsum and the formation of a highly cross-linked silica-rich gel were noted.

The results here fill the knowledge gap for the sulfuric acid resistance of the Fe-rich alkali-activation system. Although AA-NFS shows lower sulfuric acid resistance compared to cement, the permeability and porosity of cement are much lower than the AA-NFS developed herein,

629 so the comparison is not fair as it is based on different initial pore structures. Future work could

630 focus on how to reduce pores and permeability of AA-NFS. In addition, other aspects of

631 durability performance, like organic acid resistance and sulfate salts resistance, should be

632 addressed as well.

633

637

638 ## Declaration of competing interest

639 The authors declare that they do not have any competing financial interests or personal

640 relationships that might be perceived as influencing the findings presented in this paper.

641

Reference

[1] G. Habert, S.A. Miller, V.M. John, J.L. Provis, A. Favier, A. Horvath, K.L. Scrivener, Environmental impacts and decarbonization strategies in the cement and concrete industries, Nature Reviews Earth & Environment, 1 (2020) 559-573.

[2] D. Khale, R. Chaudhary, Mechanism of geopolymerization and factors influencing its development: a review, Journal of Materials Science, 42 (2007) 729-746.

[3] P.S. Deb, P. Nath, P.K. Sarker, The effects of ground granulated blast-furnace slag blending with fly ash and activator content on the workability and strength properties of geopolymer concrete cured at ambient temperature, Materials & Design (1980-2015), 62 (2014) 32-39.

[4] A. Peys, V. Isteri, J. Yliniemi, A.S. Yorkshire, P.N. Lemougna, C. Utton, J.L. Provis, R. Snellings, T. Hanein, Sustainable iron-rich cements: Raw material sources and binder types, Cement and Concrete Research, 157 (2022) 106834.

[5] J. Van De Sande, A. Peys, T. Hertel, H. Rahier, Y. Pontikes, Upcycling of non-ferrous metallurgy slags: Identifying the most reactive slag for inorganic polymer construction materials, Resources, Conservation and Recycling, 154 (2020) 104627.

[6] G. Ascensão, F. Faleschini, M. Marchi, M. Segata, J. Van De Sande, H. Rahier, E. Bernardo, Y. Pontikes, High-Temperature Behavior of CaO-FeOx-Al2O3-SiO2-Rich Alkali Activated Materials, Applied Sciences, 12 (2022) 2572.

[7] A. Peys, A.P. Douvalis, V. Hallet, H. Rahier, B. Blanpain, Y. Pontikes, Inorganic Polymers From CaO-FeOx-SiO2 Slag: The Start of Oxidation of Fe and the Formation of a Mixed Valence Binder, Frontiers in Materials, 6 (2019).

[8] J. Monteny, E. Vincke, A. Beeldens, N. De Belie, L. Taerwe, D. Van Gemert, W. Verstraete, Chemical, microbiological, and in situ test methods for biogenic sulfuric acid corrosion of concrete, Cement and Concrete Research, 30 (2000) 623-634.

[9] E. Álvarez-Ayuso, X. Querol, F. Plana, A. Alastuey, N. Moreno, M. Izquierdo, O. Font, T. Moreno, S. Diez, E. Vázquez, M. Barra, Environmental, physical and structural characterisation of geopolymer matrixes synthesised from coal (co-)combustion fly ashes, Journal of Hazardous Materials, 154 (2008) 175-183.

[10] C. Grengg, F. Mittermayr, A. Baldermann, M.E. Böttcher, A. Leis, G. Koraimann, P. Grunert, M. Dietzel, Microbiologically induced concrete corrosion: A case study from a combined sewer network, Cement and Concrete Research, 77 (2015) 16-25.

[11] M.T. Bassuoni, M.L. Nehdi, Resistance of self-consolidating concrete to sulfuric acid attack with consecutive pH reduction, Cement and Concrete Research, 37 (2007) 1070-1084.

[12] S.A. Bernal, E.D. Rodríguez, R. Mejía de Gutiérrez, J.L. Provis, Performance of alkali-activated slag mortars exposed to acids, Journal of Sustainable Cement-Based Materials, 1 (2012) 138-151.

[13] K. Gong, C.E. White, Nanoscale Chemical Degradation Mechanisms of Sulfate Attack in Alkali-activated Slag, The Journal of Physical Chemistry C, 122 (2018) 5992-6004.

[14] A. Gruskovnjak, B. Lothenbach, F. Winnefeld, R. Figi, S.C. Ko, M. Adler, U. Mäder, Hydration mechanisms of super sulphated slag cement, Cement and Concrete Research, 38 (2008) 983-992.

[15] S. Caijun, L. Yinyu, Investigation on some factors affecting the characteristics of alkali-phosphorus slag cement, Cement and Concrete Research, 19 (1989) 7.

[16] V. Pavlik, CORROSION OF HARDENED CEMENT PASTE BY ACETIC AND NITRIC ACIDS - PART I: CALCULATION OF CORROSION DEPTH, Cement and Concrete Research, 24 (1994) 12.

[17] J. Singh, S.P. Singh, Geopolymerization of solid waste of non-ferrous metallurgy - A review, J Environ Manage, 251 (2019) 109571.

690 [18] A. Wang, Y. Zheng, Z. Zhang, K. Liu, Y. Li, L. Shi, D. Sun, The Durability of Alkali-
691 Activated Materials in Comparison with Ordinary Portland Cements and Concretes: A Review,
692 Engineering, 6 (2020) 695-706.
693 [19] H. Sreenivasan, E. Adesanya, H. Niu, P. Perumal, A.M. Kantola, V.-V. Telkki, M. Huttula,
694 W. Cao, J.L. Provis, M. Illikainen, P. Kinnunen, Evidence of formation of an amorphous
695 magnesium silicate (AMS) phase during alkali activation of (Na-Mg) aluminosilicate glasses,
696 Cement and Concrete Research, 145 (2021).
697 [20] A. Koenig, A. Herrmann, S. Overmann, F. Dehn, Resistance of alkali-activated binders to
698 organic acid attack: Assessment of evaluation criteria and damage mechanisms, Construction
699 and Building Materials, 151 (2017) 405-413.
700 [21] V. Ponomar, J. Yliniemi, E. Adesanya, K. Ohenoja, M. Illikainen, An overview of the
701 utilisation of Fe-rich residues in alkali-activated binders: Mechanical properties and state of
702 iron, Journal of Cleaner Production, 330 (2022).
703 [1] G. Habert, S.A. Miller, V.M. John, J.L. Provis, A. Favier, A. Horvath, K.L. Scrivener,
704 Environmental impacts and decarbonization strategies in the cement and concrete industries,
705 Nature Reviews Earth & Environment, 1 (2020) 559-573.
706 [2] D. Khale, R. Chaudhary, Mechanism of geopolymerization and factors influencing its
707 development: a review, Journal of Materials Science, 42 (2007) 729-746.
708 [3] P.S. Deb, P. Nath, P.K. Sarker, The effects of ground granulated blast-furnace slag blending
709 with fly ash and activator content on the workability and strength properties of geopolymer
710 concrete cured at ambient temperature, Materials & Design (1980-2015), 62 (2014) 32-39.
711 [4] A. Peys, V. Isteri, J. Yliniemi, A.S. Yorkshire, P.N. Lemougna, C. Utton, J.L. Provis, R.
712 Snellings, T. Hanein, Sustainable iron-rich cements: Raw material sources and binder types,
713 Cement and Concrete Research, 157 (2022) 106834.
714 [5] J. Van De Sande, A. Peys, T. Hertel, H. Rahier, Y. Pontikes, Upcycling of non-ferrous
715 metallurgy slags: Identifying the most reactive slag for inorganic polymer construction
716 materials, Resources, Conservation and Recycling, 154 (2020) 104627.
717 [6] G. Ascensão, F. Faleschini, M. Marchi, M. Segata, J. Van De Sande, H. Rahier, E. Bernardo,
718 Y. Pontikes, High-Temperature Behavior of CaO-FeOx-Al2O3-SiO2-Rich Alkali Activated
719 Materials, Applied Sciences, 12 (2022) 2572.
720 [7] A. Peys, A.P. Douvalis, V. Hallet, H. Rahier, B. Blanpain, Y. Pontikes, Inorganic Polymers
721 From CaO-FeOx-SiO2 Slag: The Start of Oxidation of Fe and the Formation of a Mixed
722 Valence Binder, Frontiers in Materials, 6 (2019).
723 [8] J. Monteny, E. Vincke, A. Beeldens, N. De Belie, L. Taerwe, D. Van Gemert, W. Verstraete,
724 Chemical, microbiological, and in situ test methods for biogenic sulfuric acid corrosion of
725 concrete, Cement and Concrete Research, 30 (2000) 623-634.
726 [9] E. Álvarez-Ayuso, X. Querol, F. Plana, A. Alastuey, N. Moreno, M. Izquierdo, O. Font, T.
727 Moreno, S. Diez, E. Vázquez, M. Barra, Environmental, physical and structural
728 characterisation of geopolymer matrixes synthesised from coal (co-)combustion fly ashes,
729 Journal of Hazardous Materials, 154 (2008) 175-183.
730 [10] C. Grengg, F. Mittermayr, A. Baldermann, M.E. Böttcher, A. Leis, G. Koraimann, P.
731 Grunert, M. Dietzel, Microbiologically induced concrete corrosion: A case study from a
732 combined sewer network, Cement and Concrete Research, 77 (2015) 16-25.
733 [11] M.T. Bassuoni, M.L. Nehdi, Resistance of self-consolidating concrete to sulfuric acid
734 attack with consecutive pH reduction, Cement and Concrete Research, 37 (2007) 1070-1084.
735 [12] S.A. Bernal, E.D. Rodríguez, R. Mejía de Gutiérrez, J.L. Provis, Performance of alkali-
736 activated slag mortars exposed to acids, Journal of Sustainable Cement-Based Materials, 1
737 (2012) 138-151.
738 [13] K. Gong, C.E. White, Nanoscale Chemical Degradation Mechanisms of Sulfate Attack in
739 Alkali-activated Slag, The Journal of Physical Chemistry C, 122 (2018) 5992-6004.

740 [14] A. Gruskovnjak, B. Lothenbach, F. Winnefeld, R. Figi, S.C. Ko, M. Adler, U. Mäder,
741 Hydration mechanisms of super sulphated slag cement, Cement and Concrete Research, 38
742 (2008) 983-992.
743 [15] S. Caijun, L. Yinyu, Investigation on some factors affecting the characteristics of alkali-
744 phosphorus slag cement, Cement and Concrete Research, 19 (1989) 7.
745 [16] V. Pavlik, CORROSION OF HARDENED CEMENT PASTE BY ACETIC AND
746 NITRIC ACIDS - PART I: CALCULATION OF CORROSION DEPTH, Cement and
747 Concrete Research, 24 (1994) 12.
748 [17] J. Singh, S.P. Singh, Geopolymerization of solid waste of non-ferrous metallurgy - A
749 review, J Environ Manage, 251 (2019) 109571.
750 [18] A. Wang, Y. Zheng, Z. Zhang, K. Liu, Y. Li, L. Shi, D. Sun, The Durability of Alkali-
751 Activated Materials in Comparison with Ordinary Portland Cements and Concretes: A Review,
752 Engineering, 6 (2020) 695-706.
753 [19] H. Sreenivasan, E. Adesanya, H. Niu, P. Perumal, A.M. Kantola, V.-V. Telkki, M. Huttula,
754 W. Cao, J.L. Provis, M. Illikainen, P. Kinnunen, Evidence of formation of an amorphous
755 magnesium silicate (AMS) phase during alkali activation of (Na-Mg) aluminosilicate glasses,
756 Cement and Concrete Research, 145 (2021).
757 [20] A. Koenig, A. Herrmann, S. Overmann, F. Dehn, Resistance of alkali-activated binders to
758 organic acid attack: Assessment of evaluation criteria and damage mechanisms, Construction
759 and Building Materials, 151 (2017) 405-413.
760 [21] V. Ponomar, J. Yliniemi, E. Adesanya, K. Ohenoja, M. Illikainen, An overview of the
761 utilisation of Fe-rich residues in alkali-activated binders: Mechanical properties and state of
762 iron, Journal of Cleaner Production, 330 (2022).
763 [22] A.A. Adediran, J. Yliniemi, V. Carvelli, E. Adesanya, M. Illikainen, Durability of Alkali-
764 Activated Fe-Rich Fayalite Slag-Based Mortars Subjected to Different Environmental
765 Conditions, Cement and Concrete Research, (2022).
766 [23] M. Ben Haha, B. Lothenbach, G. Le Saout, F. Winnefeld, Influence of slag chemistry on
767 the hydration of alkali-activated blast-furnace slag — Part I: Effect of MgO, Cement and
768 Concrete Research, 41 (2011) 955-963.
769 [24] S.A. Bernal, R. San Nicolas, R.J. Myers, R. Mejía de Gutiérrez, F. Puertas, J.S.J. van
770 Deventer, J.L. Provis, MgO content of slag controls phase evolution and structural changes
771 induced by accelerated carbonation in alkali-activated binders, Cement and Concrete Research,
772 57 (2014) 33-43.
773 [25] S.A. Walling, S.A. Bernal, L.J. Gardner, H. Kinoshita, J.L. Provis, Phase Formation and
774 Evolution in Mg(OH)2–Zeolite Cements, Industrial & Engineering Chemistry Research, 57
775 (2018) 2105-2113.
776 [26] Y.J. Zhang, Y.L. Zhao, H.H. Li, D.L. Xu, Structure characterization of hydration products
777 generated by alkaline activation of granulated blast furnace slag, Journal of Materials Science,
778 43 (2008) 7141-7147.
779 [27] J.P. Gevaudan, Z. Craun, W.V. Srubar, Sulfuric acid degradation of alkali-activated
780 metakaolin cements supplemented with brucite, Cement and Concrete Composites, 121 (2021).
781 [28] A.B. E. Douglas, V.M. Malhotra, Properties and Durability of Alkali-Activated Slag
782 Concrete, ACI Materials Journal, 89.
783 [29] A. Allahverdi, F. Škvára, Sulfuric acid attack on hardened paste of geopolymer cements
784 part 1. Mechanism of corrosion at relatively high concentrations, Ceramics - Silikaty, 49 (2005)
785 225-229.
786 [30] J. Aliques-Granero, T.M. Tognonvi, A. Tagnit-Hamou, Durability test methods and their
787 application to AAMs: case of sulfuric-acid resistance, Materials and Structures, 50 (2016).
788 [31] R.R. Lloyd, J.L. Provis, J.S.J. van Deventer, Acid resistance of inorganic polymer binders.
789 1. Corrosion rate, Materials and Structures, 45 (2011) 1-14.

[32] P.S. Deb, P.K. Sarker, S. Barbhuiya, Sorptivity and acid resistance of ambient-cured geopolymer mortars containing nano-silica, Cement and Concrete Composites, 72 (2016) 235-245.

[33] J.S.J. van Deventer, J.L. Provis, P. Duxson, D.G. Brice, Chemical Research and Climate Change as Drivers in the Commercial Adoption of Alkali Activated Materials, Waste and Biomass Valorization, 1 (2010) 145-155.

[34] J.L. Provis, J.S.J.v. Deventer, Alkali-Activated Materials: State-of-the-Art Report, Rilem TC 224-AAM, Springer/RILEM, Dordrecht, The Netherlands, (2014).

[35] C. Siakati, A.P. Douvalis, A. Peys, Y. Pontikes, Binary, ternary and quaternary Fe-rich slags: Influence of Fe and Si substitution by Ca and Al on the atomic structure and reactivity, Conference: 6th International Slag Valorisation Symposium, (2019).

[36] N. Wen, A. Peys, T. Hertel, V. Hallet, Y. Pontikes, Slag or Reacted Binder, Which Dissolves First in Sulphuric Acid?, International RILEM Conference on Synergising Expertise towards Sustainability and Robustness of Cement-based Materials and Concrete Structures2023, pp. 715-722.

[37] Y. Ma, G. Wang, G. Ye, J. Hu, A comparative study on the pore structure of alkali-activated fly ash evaluated by mercury intrusion porosimetry, N2 adsorption and image analysis, Journal of Materials Science, 53 (2018) 5958-5972.

[38] N.N. Naik, A.C. Jupe, S.R. Stock, A.P. Wilkinson, P.L. Lee, K.E. Kurtis, Sulfate attack monitored by microCT and EDXRD: Influence of cement type, water-to-cement ratio, and aggregate, Cement and Concrete Research, 36 (2006) 144-159.

[39] Z. Yu, R. Oliveira-Silva, E.D. Oliveira, N. Wen, Y. Pontikes, D. Sakellariou, An In-situ Method for Assessing the Kinetics of Acid Attack on Iron-rich Alkali-activated Materials, 16th International Conference on Durability of Building Materials and Components, (2023).

[40] A. Peys, A.P. Douvalis, C. Siakati, H. Rahier, B. Blanpain, Y. Pontikes, The influence of air and temperature on the reaction mechanism and molecular structure of Fe-silicate inorganic polymers, Journal of Non-Crystalline Solids, 526 (2019).

[41] R.L. Hartman, H.S. Fogler, The Unique Mechanism of Analcime Dissolution by Hydrogen Ion Attack, Langmuir, 22 (2006) 11163-11170.

[42] P.K. Holt, G.W. Barton, M. Wark, C.A. Mitchell, A quantitative comparison between chemical dosing and electrocoagulation, Colloids and Surfaces A: Physicochemical and Engineering Aspects, 211 (2002) 233-248.

[43] C. Grengg, G.J.G. Gluth, F. Mittermayr, N. Ukrainczyk, M. Bertmer, A. Guilherme Buzanich, M. Radtke, A. Leis, M. Dietzel, Deterioration mechanism of alkali-activated materials in sulfuric acid and the influence of Cu: A micro-to-nano structural, elemental and stable isotopic multi-proxy study, Cement and Concrete Research, 142 (2021).

[44] V.C. Farmer, D.G. Lumsdon, An assessment of complex formation between aluminium and silicic acid in acidic solutions, Geochimica et Cosmochimica Acta, 58 (1994) 3331-3334.

[45] H. Wonisch, F. Gérard, M. Dietzel, J. Jaffrain, O. Nestroy, J.P. Boudot, Occurrence of polymerized silicic acid and aluminum species in two forest soil solutions with different acidity, Geoderma, 144 (2008) 435-445.

[46] A. ALLAHVERDI, F. ŠKVÁRA, Sulfuric acid attack on hardened paste of geopolymer cements - Part 1. Mechanism of corrosion at relatively, Ceramics − Silikáty, 49 (2005) 5.

[47] P. Sturm, G.J.G. Gluth, C. Jäger, H.J.H. Brouwers, H.C. Kühne, Sulfuric acid resistance of one-part alkali-activated mortars, Cement and Concrete Research, 109 (2018) 54-63.

[48] S. Onisei, A.P. Douvalis, A. Malfliet, A. Peys, Y. Pontikes, Inorganic polymers made of fayalite slag: On the microstructure and behavior of Fe, Journal of the American Ceramic Society, 101 (2018) 2245-2257.

[49] T. Bakharev, Resistance of geopolymer materials to acid attack, Cement and Concrete Research, 35 (2005) 658-670.

840 [50] C. Siakati, A.P. Douvalis, V. Hallet, A. Peys, Y. Pontikes, Influence of CaO/FeO ratio on
841 the formation mechanism and properties of alkali-activated Fe-rich slags, Cement and Concrete
842 Research, 146 (2021).
843 [51] A. Fidalgo, L.M. Ilharco, The defect structure of sol−gelderived silicapolytetrahydrofuran
844 hybrid films by FTIR, Journal of Non-Crystalline Solids 283 (2001) 11.
845 [52] R. Al-Oweini, H. El-Rassy, Synthesis and characterization by FTIR spectroscopy of silica
846 aerogels prepared using several Si(OR)4 and R′′Si(OR′)3 precursors, Journal of Molecular
847 Structure, 919 (2009) 140-145.
848 [53] S. Palacio, M. Aitkenhead, A. Escudero, G. Montserrat-Marti, M. Maestro, A.H.
849 Robertson, Gypsophile chemistry unveiled: Fourier transform infrared (FTIR) spectroscopy
850 provides new insight into plant adaptations to gypsum soils, PLoS One, 9 (2014) e107285.
851 [54] B. Walkley, J.L. Provis, Solid-state nuclear magnetic resonance spectroscopy of cements,
852 Materials Today Advances, 1 (2019) 100007.
853 [55] M.R. Jones, D.E. Macphee, J.A. Chudek, G. Hunter, R. Lannegrand, R. Talero, S.N.
854 Scrimgeour, Studies using 27Al MAS NMR of AFm and AFt phases and the formation of
855 Friedel's salt, Cement and Concrete Research, 33 (2003) 177-182.
856 [56] A. Peys, C.E. White, H. Rahier, B. Blanpain, Y. Pontikes, Alkali-activation of CaO-FeOx-
857 SiO2 slag: Formation mechanism from in-situ X-ray total scattering, Cement and Concrete
858 Research, 122 (2019) 179-188.
859 [57] Y. Wang, Y. Cao, Z. Zhang, J. Huang, P. Zhang, Y. Ma, H. Wang, Study of acidic
860 degradation of alkali-activated materials using synthetic C-(N)-A-S-H and N-A-S-H gels,
861 Composites Part B: Engineering, 230 (2022) 109510.
862 [58] T. Gutberlet, H. Hilbig, R.E. Beddoe, Acid attack on hydrated cement — Effect of mineral
863 acids on the degradation process, Cement and Concrete Research, 74 (2015) 35-43.
864 [59] M.A. Longhi, B. Walkley, E.D. Rodríguez, A.P. Kirchheim, Z. Zhang, H. Wang, New
865 selective dissolution process to quantify reaction extent and product stability in metakaolin-
866 based geopolymers, Composites Part B: Engineering, 176 (2019) 107172.
867 [60] R.J. Myers, S.A. Bernal, R. San Nicolas, J.L. Provis, Generalized Structural Description
868 of Calcium–Sodium Aluminosilicate Hydrate Gels: The Cross-Linked Substituted Tobermorite
869 Model, Langmuir, 29 (2013) 5294-5306.
870 [61] W. Lutz, D. Heidemann, C. Hübert, W. Wieker, Contribution of silica gels to
871 superimposed 29Si MAS NMR spectra of Y zeolites dealuminated by steaming, Zeitschrift für
872 anorganische und allgemeine Chemie, 627 (2001) 2559-2564.
873 [62] N. WEN, A. PEYS, T. HERTEL, Y. PONTIKES, Impact of Ca, Al, and Mg on reaction
874 kinetics, pore structure and performance of Fe-rich alkali-activated slag, Journal of the
875 American Ceramic Society, Accepted in Janurary 2024 (2024).
876
877
878
879
880